JOURNAL OF GEOPHYSICAL RESEARCH, VOL. 117, D00U12, doi:10.1029/2011JD016688, 2012

A case study of observations of volcanic ash from the Eyjafjallajökull eruption: 1. In situ airborne observations

Kate Turnbull,[1] Ben Johnson,[1] Franco Marenco,[1] Jim Haywood,[1,2] Andreas Minikin,[3] Bernadett Weinzierl,[3] Hans Schlager,[3] Ulrich Schumann,[3] Susan Leadbetter,[4] and Alan Woolley[5]

Received 15 August 2011; revised 16 November 2011; accepted 17 November 2011; published 14 February 2012.

[1] On 17 May 2010, the FAAM BAe-146 aircraft made remote and in situ measurements of the volcanic ash cloud from Eyjafjallajökull over the southern North Sea. The Falcon 20E aircraft operated by Deutsches Zentrum für Luft- und Raumfahrt (DLR) also sampled the ash cloud on the same day. While no "wingtip-to-wingtip" co-ordination was performed, the proximity of the two aircraft allows worthwhile comparisons. Despite the high degree of inhomogeneity (e.g., column ash loadings varied by a factor of three over ~100 km) the range of ash mass concentrations and the ratios between volcanic ash mass and concentrations of SO_2, O_3 and CO were consistent between the two aircraft and within expected instrumental uncertainties. The data show strong correlations between ash mass, SO_2 concentration and aerosol scattering with the FAAM BAe-146 data providing a specific extinction coefficient of 0.6–0.8 $m^2\ g^{-1}$. There were significant differences in the observed ash size distribution with FAAM BAe-146 data showing a peak in the mass at ~3.5 μm (volume-equivalent diameter) and DLR data peaking at ~10 μm. Differences could not be accounted for by refractive index and shape assumptions alone. The aircraft in situ and lidar data suggest peak ash concentrations of 500–800 $\mu g\ m^{-3}$ with a factor of two uncertainty. Comparing the location of ash observations with the ash dispersion model output highlights differences that demonstrate the difficulties in forecasting such events and the essential nature of validating models using high quality observational data from platforms such as the FAAM BAe-146 and the DLR Falcon.

Citation: Turnbull, K., B. Johnson, F. Marenco, J. Haywood, A. Minikin, B. Weinzierl, H. Schlager, U. Schumann, S. Leadbetter, and A. Woolley (2012), A case study of observations of volcanic ash from the Eyjafjallajökull eruption: 1. In situ airborne observations, *J. Geophys. Res.*, *117*, D00U12, doi:10.1029/2011JD016688.

1. Introduction

[2] During the period between 14 April 2010 and 21 May 2010, the explosive eruption of the Icelandic volcano, Eyjafjallajökull, caused extensive disruption to the aviation industry. The economic cost to the aviation industry has been estimated to be in the region of $320 m per day (e.g., http://news.bbc.co.uk/1/hi/uk/8624663.stm) with subsequent estimates of the impact on the global economy around U.S. $5bn (http://www.airbus.com/fileadmin/media_gallery/files/other/Volcanic-Update.pdf). The main concern for air traffic is that at sufficiently large concentrations, ash particles have been known to damage aircraft engines, and can lead to in flight engine failure with potentially catastrophic consequences [*Guffanti et al.*, 2010; *Witham et al.*, 2012]. *Webley and Mastin* [2009] suggest that over 120 aircraft have inadvertently flown through clouds of volcanic ash from explosive volcanic eruptions with varying degrees of damage reported.

[3] Despite the huge potential financial consequences for air-traffic, in situ airborne atmospheric research into volcanic ash clouds is, understandably, limited owing to safety concerns for the suitably equipped atmospheric research aircraft. *Carn et al.* [2011] and *Schumann et al.* [2011] provide a review of airborne sampling activities before the Eyjafjallajökull event. Recent airborne measurements include the sampling of the high latitude explosive eruptions of Hekla, Iceland, 2000 by *Hunton et al.* [2005] and *Rose et al.* [2006], and the sampling of the eruption from Erebus, Antarctica in 2007 by *Oppenheimer et al.* [2010].

[4] Subsequent to the Eyjafjallajökull eruption and the closure of airspace, it became immediately apparent that in

[1]Observation Based Research, Met Office, Exeter, UK.
[2]College of Engineering, Mathematics, and Physical Science, University of Exeter, Exeter, UK.
[3]Institut für Physik der Atmosphäre, Deutsches Zentrum für Luft- und Raumfahrt, Oberpfaffenhofen, Germany.
[4]Atmospheric Dispersion, Met Office, Exeter, UK.
[5]Facility for Airborne Atmospheric Measurements, Cranfield, UK.

0148-0227/12/2011JD016688

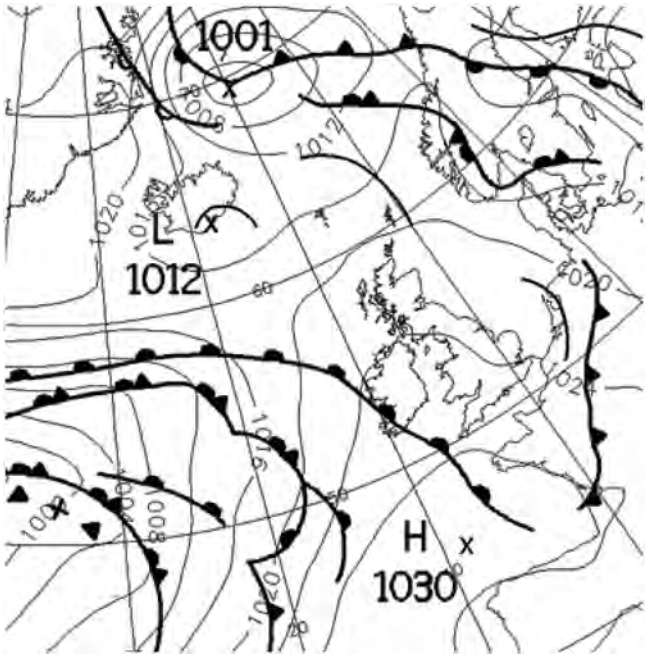

Figure 1. Synoptic analysis from UK Met Office at 12:00 UTC on 17 May 2010.

situ and remote sensing measurements by dedicated atmospheric research aircraft were urgently required to validate volcanic ash dispersion forecasts. Among the European research aircraft that were mobilized for these measurements were the UK's BAe-146-301 Atmospheric Research Aircraft managed by the Facility for Airborne Atmospheric Measurements (FAAM http://www.faam.ac.uk) and Germany's DLR Falcon aircraft (http://www.dlr.de) [*Schumann et al.*, 2011]. A total of 12 flights were carried out by the FAAM aircraft (see B. T. Johnson et al., In situ observations of volcanic ash clouds from the FAAM aircraft during the eruption of Eyjafjallajökull in 2010, submitted to *Journal of Geophysical Research*, 2011, for further details), and a total of 17 flights were performed by the DLR Falcon (see *Schumann et al.*, 2011 for further details). While Johnson et al. (submitted manuscript, 2011), *Marenco et al.* [2011] and *Schumann et al.* [2011] provide an overview and some highlights of the measurements made, here we concentrate in detail on measurements from 17 May 2010 when both aircraft were operating over the southern North Sea targeting volcanic ash. Section 2 describes the meteorological situation that led to the advection of the ash cloud over UK airspace on that day, sections 3 and 4 describe the instrumentation onboard the BAe-146 and the DLR Falcon respectively, and section 5 details the flight patterns that were flown by the two aircraft. After presenting results in section 6, these are discussed and conclusions drawn in section 7.

[5] The data from radiometric instruments during this flight as well as a comparison with Infrared Atmospheric Sounding Interferometer (IASI) satellite data is explored in the companion paper by *Newman et al.* [2012].

2. Prevailing Meteorology and Ash Dispersion

[6] The meteorological surface analysis for 12:00 UTC on 17 May 2010 (Figure 1) shows a ridge of high pressure with its axis over the UK and set to gradually progress eastward. Light north to northwesterly winds extending from Iceland over the eastern UK and North Sea were forecast to carry the volcanic ash cloud toward the Shetland Isles then south toward the Netherlands and northern Germany. Conditions in the southern North Sea were predominantly cloud-free following the clearance of the trough lying over the Benelux countries at 12:00 UTC and ahead of upper-level cloud associated with the warm front approaching from the west.

[7] Forecasts of regions of significant ash concentration issued by the London Volcanic Ash Advisory Centre (VAAC) are produced using the Met Office Numerical Atmospheric dispersion Modeling Environment (NAME) [*Jones et al.*, 2007]. During the Eyjafjallajökull eruption, the driving meteorology was taken from forecasts obtained from the global version of the Met Office's NWP model (the Unified Model) [*Webster et al.*, 2012]. The modeled loss processes for volcanic ash within NAME are wet and dry deposition and gravitational settling of heavy particles. A particle size distribution based on measurements of volcanic ash by *Hobbs et al.* [1991] is used. Particles larger than 100 μm are assumed to fall out near to the source and are therefore not included.

[8] Forecasts of expected peak volcanic ash concentrations were provided to the aviation industry over three layers during the Eyjafjallajökull event; the surface to FL200 (roughly surface-6 km), FL200-FL350 (approximately 6–10 km) and FL350-FL550 (above 10 km), where each unit FL (flight level) is equivalent to 100 feet assuming the International Civil Aviation Organization (ICAO) standard atmosphere. In this case study, the majority of volcanic ash was forecast in the lowest of these layers. Figure 2 shows the forecast peak volcanic ash concentrations from FL000-FL200 for 12:00–18:00 UTC on 17 May 2010.

[9] Figure 2 shows the ash cloud extending from Iceland southeastward over the UK and European airspace. Black colors indicate forecast peak ash concentrations in excess of 4000 μg m^{-3} while gray is 2000–4000 μg m^{-3} and red shows concentrations between 200 μg m^{-3} and 2000 μg m^{-3}. These thresholds were selected by the UK Civil Aviation Authority (CAA) based on safety recommendations from aircraft engine manufacturers. The model output shown in Figure 2 is based on a post-event model re-run where analyzed, rather than forecast, meteorological fields have been used [*Webster et al.*, 2012]. A version of this product based on forecast meteorology and using a different color scale has been shown by *Schumann et al.* [2011].

[10] Satellite products are also extremely useful in both qualitatively assessing the location of the volcanic ash cloud and in quantitatively assessing the column loading, altitude, and atmospheric concentration of the volcanic ash [*Newman et al.*, 2012]. The Spinning Enhanced Visible and Infra-Red Imager (SEVIRI) instrument on the Meteosat Second Generation (MSG) geostationary satellite dust RGB product (http://oiswww.eumetsat.org/IPPS/html/MSG/RGB) proved particularly useful in this respect because qualitative data was available at 15 min intervals, which far exceeds the temporal frequency of polar orbiting satellite retrievals. However, the interpretation of ash in the SEVIRI imagery can become ambiguous in certain atmospheric conditions, for example when aerosol optical depths are low or when the atmosphere is moist and/or cloudy. More specific volcanic

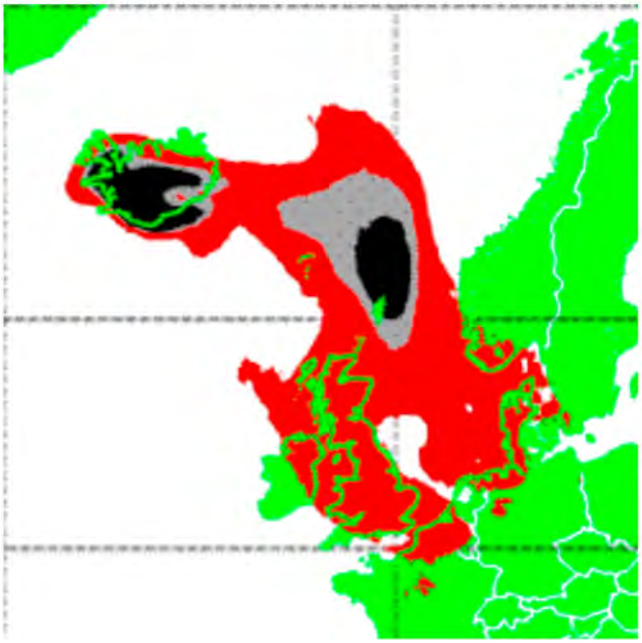

Figure 2. NAME modeled peak ash concentrations for FL000-FL200 for 12:00–18:00 UTC, on 17 May 2010. Black colors indicate forecast peak concentrations in excess of 4000 μg m^{-3}, gray is 2000–4000 μg m^{-3} and red is 200–2000 μg m^{-3}.

ash retrieval methods for the SEVIRI instrument are explored by *Francis et al.* [2012] and A. J. Prata and A. T. Prata (Eyjafjallajökull volcanic ash concentrations derived from SEVIRI measurements, submitted to *Journal of Geophysical Research*, 2012), while those for the Moderate Resolution Imaging Spectroradiometer (MODIS) and the Ozone Monitoring Instrument (OMI) are investigated by S. Christopher et al. (Eyjafjallajokull volcanic ash cloud over the North Sea during May 4–May 18, 2010, submitted to *Journal of Geophysical Research*, 2012). Figure 3 shows images from 14:00 UTC and 17:00 UTC; the volcanic ash is indicated in bright orange colors, while low clouds are dark orange, mid-level clouds are green and the high-level cloud associated with the approaching warm front are red-brown. It should be noted that the color that ash appears in this type of satellite imagery will vary from case to case depending on plume height and ash properties [*Millington et al.*, 2012].

[11] Figure 3 indicates the presence of volcanic ash over the North Sea and that, between 14:00 UTC and 17:00 UTC, the forward edge of the ash cloud advected south-southeast by approximately 100 km. Comparing Figures 2 and 3 shows that the position of the eastern section of the ash cloud over the North Sea is reasonably captured by the model, although the model may not have brought it quite far enough south and west. In contrast, the western section of the modeled ash cloud over the UK appears to be absent in the satellite imagery. By using improved source term estimations of the ash emissions derived with an inversion technique that constrains modeled ash emission with SEVIRI satellite observations in the NAME model, *Kristiansen et al.* [2012] achieved model output that is in better agreement with observations. In particular, the western section of the modeled ash cloud over the UK was no longer evident in the modeled total ash column loading, suggesting that deficiencies in the original model source term may have contributed to the differences between Figures 2 and 3. This clearly demonstrates the value of the satellite imagery in assessing the model forecasts.

3. FAAM BAe-146 Operations and Instrumentation

[12] As a turbine driven aircraft, the FAAM BAe-146 aircraft was subject to the same safety concerns as the rest of civil aviation and was prohibited from flying in areas where forecast concentrations exceeded 2000 μg m^{-3}. Additional safety criteria relating to the exposure to sulphur dioxide (SO_2) were also applied by the aircraft operators. During the Eyjafjallajökull eruption event, the BAe-146 specifically

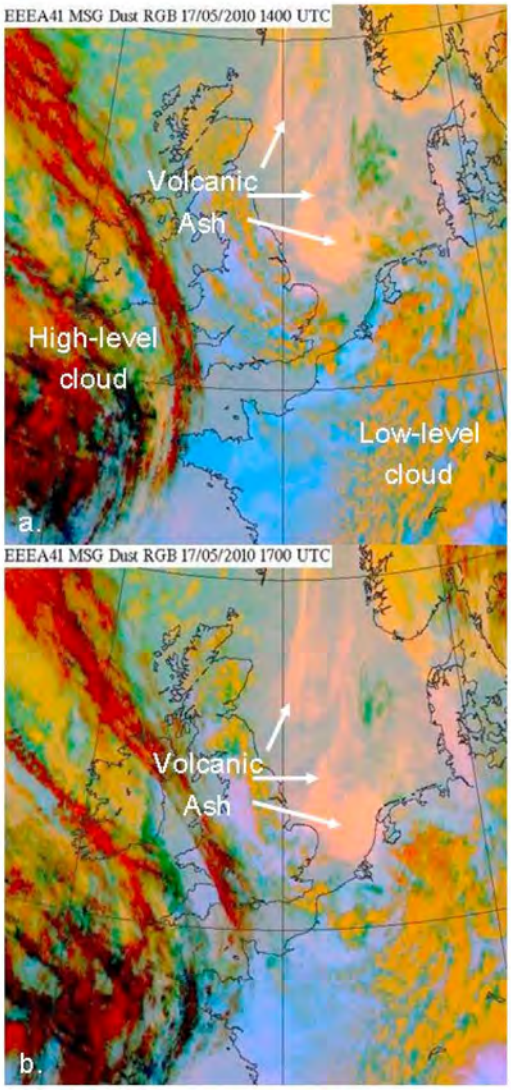

Figure 3. RGB dust product from SEVIRI instrument on the MSG satellite for (a) 14:00 UTC and (b) 17:00 UTC on 17 May 2010. For this eruption, the volcanic ash is indicated in bright orange colors, while low clouds are dark orange and high-level cloud is red-brown.

Table 1. Instruments on the FAAM BAe-146 and the DLR Falcon on 17 May 2010 Used in This Case Study[a]

	FAAM BAe-146	DLR Falcon
Coarse particles	CAS (0.6–50 μm, wing-mounted)	FSSP-300 (0.3–20 μm, wing-mounted, lowest and highest bins rejected)
Fine particles	PCASP-100X (0.1–3 μm, dry, wing, lowest bin rejected).	PCASP-100X (0.1–3 μm, dry, wing, lowest bins rejected)
SO_2	TECO 43C Trace Level	TECO 43C Trace Level
O_3	TECO 49C	TECO 49C
CO	Aerolaser AL 5002	Aerolaser AL 5001
Lidar	Leosphere 'EZ' lidar 355 nm, nadir-viewing.	*2-μm Doppler wind lidar* (*conical scans, not used*)
Scattering	Nephelometer TSI-3563, 3 wavelength.	-

[a]Note that given size ranges are in terms of the standard calibration, i.e., spherical water drops for CAS and FSSP and polystyrene latex spheres (PSLs) for the PCASPs. Italics indicate an instrument that was fitted and operated but has not been used in this work.

targeted forecast 'red zones' (200–2000 μg m^{-3}) in order to gather in situ measurements of the volcanic ash cloud and validate the NAME model products. While dispersion forecasts provided information on the progression and spatial distribution of the ash cloud at 6-hourly intervals, satellite imagery was also utilized in both the flight planning process and during the flight. SEVIRI RGB images such as those shown in Figure 3 were available in flight and provided additional guidance on optimal flight routing.

[13] In situ and remote sensing measurements available on the FAAM BAe-146 aircraft and the DLR Falcon that are used in this work are compared in Table 1. Instrumentation on the FAAM BAe-146 is described below.

3.1. In Situ Sampling Instrumentation

3.1.1. Particle Size Distribution Measurements

[14] From the FAAM aircraft data, the size distribution of the volcanic aerosol is derived from measurements made by two wing-mounted Optical Particle Counters (OPC). Aerosol size distributions for particles with diameter between 0.1 and 3.0 μm were determined with a Passive Cavity Aerosol Spectrometer Probe 100X (PCASP) upgraded to 30 bins with SPP200 electronics (Particle Measurement Systems originally, upgrade by Droplet Measurement Technologies (DMT) Inc., Boulder, CO). The instrument was calibrated both before and after the volcano flights.

[15] For particles with nominal diameter between 0.6 and 50 μm, a Cloud and Aerosol Spectrometer (CAS) instrument (DMT Inc., Boulder, CO) was used [*Baumgardner et al.*, 2001]. CAS is an OPC which forms part of the wing-mounted Cloud, Aerosol and Precipitation Spectrometer (CAPS) instrument. The size calibration of the instrument was checked pre-flight using glass beads and found to be within specification. All OPC measurements reported in this work are for ambient pressure and temperature.

[16] The responses of both the PCASP and CAS instruments to a particle are dependent not only on the size of that particle but also its shape and complex refractive index. The particle property assumptions used to correct the OPC data and associated optical properties are detailed by Johnson et al. (submitted manuscript, 2011), and are not discussed in depth here. For the coarse mode (0.6–35 μm) a refractive index of 1.52 + 0.0015i (based on the mineral dust data set of *Balkanski et al.* [2007], assuming a hematite level of 1.5%) is specified across all UV-visible wavelengths (355–700 nm). This is required for interpretation of lidar (355 nm), nephelometer (450, 550 and 700 nm), PCASP (630 nm) and CAS (680 nm) data. Although mineral dust is expected to have a different composition to volcanic ash, estimates for the refractive index are similar owing to the dominant silicate content. For volcanic glasses and minerals, current estimates of the real and imaginary parts are between 1.50 and 1.60 and 0.001i and 0.004i respectively for wavelengths around 600–700 nm [*Patterson*, 1981; *Patterson et al.*, 1983; *Horwell*, 2007; *Schumann et al.*, 2011]. The refractive index does not necessarily have to be the same over the entire ash size range or even for each individual ash particle. *Schumann et al.* [2011] collected volcanic ash on impactor sampling devices downstream of the DLR Falcon aerosol inlet during the flight discussed in this paper. They found that silicates constituted >95% of super-micron particles and estimated a refractive index at 632 nm (PCASP and Forward Scattering Spectrometer Probe (FSSP) wavelength) for super-micron particles to be 1.57 + 0.001i with uncertainties of 0.02 for the real part and ~factor of 3 for the imaginary part. By independently varying the real part of the refractive index between 1.50 and 1.60 and the imaginary part from 0.001i to 0.004i while contrasting spheres and the irregular shaped model for ash, Johnson et al. (submitted manuscript, 2011) estimated the uncertainty in ash mass due to the uncertainty in particle sizing arising from refractive index and shape assumptions to be a factor of 1.5. The mineral dust refractive index of *Balkanski et al.* [2007] has been used successfully to model high spectral resolution radiative measurements across the short-wave and infrared. The more strongly absorbing refractive index used by DLR in the best estimate case M (further details in section 4 and as described by *Schumann et al.* [2011]) yielded poor radiative closure [*Newman et al.*, 2012]. This gives some confidence that, though the Balkanski et al. data set is for mineral dust, it provides a reasonable assumption for the volcanic ash sampled in this case.

[17] The coarse-mode particles sampled by CAS are assumed to be irregular in shape with roughened surfaces, a choice supported by filter samples collected on the FAAM BAe-146 aircraft during in situ sampling within the volcanic ash Johnson et al. (submitted manuscript, 2011). A density of 2.3 g cm^{-3} is assumed for the coarse mode. In this work, particles in the fine mode measured by PCASP are represented by spheres with density 1.8 g cm^{-3} [*Kaye and Laby*, 1995] and a refractive index of 1.43 + 0.0000i at 550 nm, appropriate for sulphuric acid. Sulphuric acid is assumed to dominate the fine-mode species in the volcanic ash cloud. Analysis of particles collected using an impactor on the DLR Falcon found that particles inside the volcanic ash cloud consisted of a mixture of ash particles, sulphuric acid droplets or sulphate particles [*Schumann et al.*, 2011]. Other components may contribute to the fine mode but, given the presence of elevated SO_2 precursor, the refractive index and density are estimated to be near those of sulphuric acid

assumed here. Since the PCASP inlet is heated, it is expected that the aerosol will be sampled at sufficiently low humidity that it may be considered dry.

[18] To yield a single size distribution, below 0.6 μm PCASP bins 2–16 are used, while bins 2–26 from CAS provide the spectrum between 0.6 μm and 35 μm, although no ash particles with diameter larger than 25 μm (bin 24) were observed during this flight. As is shown later (section 6.1, Figure 7), agreement between the PCASP and CAS data in the size range overlap is generally reasonable.

[19] Once the corrections to the instrument bins have been made, the total mass concentration was obtained by simple summation over all measured sizes (0.1–25 μm) and ash mass concentration was calculated by summation over the coarse mode (0.6–25 μm), assuming volume-equivalent spherical diameters for each bin. For time series, 10 s averaged data is used. A full analysis of the sensitivity of the aerosol size distribution to uncertainties in refractive index, particle shape, roughness, sample volume and the resultant uncertainty in mass concentration has been carried out by Johnson et al. (submitted manuscript, 2011). Mass concentrations from the FAAM BAe-146 are estimated to have an overall uncertainty of a factor of approximately 2. A brief examination of the effect of assuming spheres on the coarse-mode mass size distribution and resultant optical properties is conducted in sections 6.1 and 6.2. Wherever ash mass is presented in Figures 6, 8, 10, 12, and 13, the default refractive index of 1.52 + 0.0015i and irregular shape have been assumed.

3.1.2. Aerosol Scattering Measurements

[20] Aerosol scattering coefficients were determined at three wavelengths (450 nm, 550 nm, 700 nm) using a TSI 3563 nephelometer via a Rosemount inlet. The 'no-cut' corrections provided by *Anderson and Ogren* [1998] were applied to correct instrument truncation and light source deficiencies. A comparison of aerosol optical depths derived from the nephelometer against AERONET Sun photometers during the Dust and Biomass burning Experiment (DABEX) [*Johnson et al.*, 2008] and the Geostationary Earth Radiation Budget Intercomparisons of Long-wave and Short-wave radiation (GERBILS) project [*Johnson and Osborne*, 2011] suggested that the majority of super-micron dust particles were sampled. An alternative suggestion might have been that the agreement indicated that over-counting of particles with diameters between e.g., 1–4 μm balances losses for particles larger than 4 μm. In this study, no a-priori correction for particle losses has been made; the validity of this assumption is investigated in section 6.5. *Johnson and Osborne* [2011] fully assessed the error in the corrected scattering coefficient derived for dust measurements using the nephelometer system on the FAAM BAe-146. They attached an overall error of $\pm$20% to the measurement, due to a combination of uncertainties in the correction factor when the Ångström exponent approaches zero, the sampling efficiency of the Rosemount inlet as a function of particle size and the effect of humidity. Data have been averaged over 10 s and are reported for ambient pressure and temperature. Drying in the inlet and instrument mean that nephelometer measurements are at sufficiently low humidity that they may be considered dry.

[21] Using optical properties calculated from OPC particle size distributions, the aerosol mass was also estimated from the scattering coefficient determined by the nephelometer. Under ideal measurement conditions, the particulate scattering coefficient, σ_{SP} (m^{-1}), is related to the total aerosol mass concentration, M (g m^{-3}), via the total mass specific scattering coefficient, k_{sca} (m^2 g^{-1}), according to equation (1)

$$M = \frac{\sigma_{SP}}{k_{sca}} \quad (1)$$

The contribution of ash to total mass (M_{ASH}) is then given by equation (2), where $w_M(c)$ is the fraction of mass attributable to the coarse mode.

$$M_{ASH} = M.\, w_M(c) \quad (2)$$

It should be noted that k_{sca} is dependent on the particle size distribution and, for the size distributions of interest here, decreases with increasing effective diameter (as also discussed by *Schumann et al.* [2011]).

3.1.3. Trace Gas Instruments

[22] Gas phase chemistry measurements of Ozone (O_3) and Carbon Monoxide (CO) were performed using a standard Thermo Electron (TECO) 49C UV photometric instrument and an UV fluorescence Aero-Laser AL5002 [*Gerbig et al.*, 1999] instrument respectively. Calibration procedures for the two gas analyzers are described by *Hopkins et al.* [2006]. Sulphur Dioxide (SO_2) was sampled using a Thermo Electron 43C Trace Level analyzer which relies on pulsed fluorescence [*Luke*, 1997].

3.2. Remote Sensing Instruments

[23] A recent addition to the capability of the FAAM BAe-146 is a nadir-viewing elastic backscatter lidar from which vertical profiles of aerosol extinction coefficient at 355 nm have been retrieved [*Marenco et al.*, 2011]. The lidar profiles presented here have a vertical resolution of 45 m and an integration time of 1 min, equivalent to an along track horizontal resolution of 8–10 km. The depolarizing lidar signal provides an additional indication of volcanic ash i.e., evidence of non-spherical particles [e.g., *Ansmann et al.*, 2010; *Marenco et al.*, 2011].

[24] From the lidar extinction profiles, the AOD from 2 km (or from cloud top, if higher) to aircraft altitude was computed. The fraction of extinction attributable to the coarse mode, f_C = 0.82 and the coarse-mode specific extinction k_{ext} = 0.72 m^2 g^{-1} at 355 nm for this flight, both derived from the CAS size-distribution, were used to convert aerosol extinction data to ash mass concentration as explained by *Marenco et al.* [2011].

[25] A comprehensive suite of radiation instruments was available on the FAAM BAe-146 aircraft and provide a unique insight into the radiative properties of the volcanic aerosol. The instruments include upward and downward facing broadband and red-domed Eppley pyranometers, the Spectral Hemispheric Integrating Measurement System (SHIMS), and the ARIES infrared interferometer. These instruments are described and the resultant measurements are presented in detail in the companion paper to this work [*Newman et al.*, 2012].

4. DLR Instrumentation

[26] The chemistry and aerosol size distribution measurements made on the DLR aircraft, as shown in Table 1, use

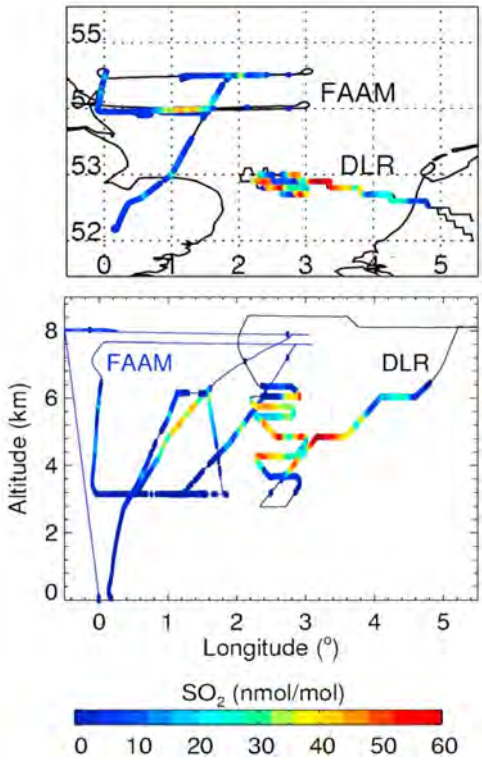

Figure 4. Flight track for FAAM BAe-146 and DLR Falcon, colored according to SO_2 concentrations (10 s averages, data below 1.0 nmol mol^{-1} not shown). (top) Geographic location. (bottom) Longitudinal cross section with height. Note that apparent steps in DLR latitude and longitude in Figure 4, top, arises from the relatively coarse (0.1°) resolution of the data.

either the same or similar instruments as the FAAM BAe-146 aircraft in most cases. However, particle size distribution measurements employed significantly different assumptions in the post-processing; details are given by *Schumann et al.* [2011]. *Schumann et al.* [2011] investigate three refractive indices with varying degrees of absorption that are expected to span the range of uncertainty in the coarse-mode size distribution. 'Case M' uses a refractive index of 1.59 + 0.004i at the FSSP laser wavelength of 633 nm and is presented as their best estimate. Case L is non-absorbing (1.59 + 0.000i) while case H is very absorbing (1.59 + 0.008i). *Schumann et al.* [2011] demonstrate that the size calibration of the instrument is more critically dependent on refractive index than particle shape for the instruments used. In their analysis, volcanic ash is assumed to be spherical. In this work, comparisons are drawn against case M since that is considered to be the DLR Falcon best estimate. The resultant size distributions from each of the three cases (L, M and H) are presented by *Schumann et al.* [2011, Figure 7].

[27] Although *Schumann et al.* [2011] assume a density of 2.6 g cm^{-3} for the entire range covered by PCASP and FSSP, for comparison with the FAAM BAe-146 size distribution, the results in this study have been adjusted to a density of 2.3 g cm^{-3} for the coarse mode and 1.8 g cm^{-3} for the fine mode. This reduces differences between post-processing applied to assumptions regarding shape and refractive index. *Schumann et al.* [2011] estimate the uncertainty in their reported mass concentration to be a factor of 2.

5. Flight Patterns

[28] The FAAM BAe-146 aircraft targeted the region in the southern North Sea where volcanic aerosol was evident on satellite imagery between 14:00 UTC and 16:30 UTC (Figure 3). In situ measurements were made in the area between 52.5 to 54.5°N and 0 to 3.0°E. Since forecast peak concentrations were below the 2000 μg m^{-3} safety threshold, in situ measurements were permitted. The lidar provided real-time qualitative information on the horizontal and vertical spatial distribution of the ash cloud. With this information, locations for vertical profiles through the ash cloud were selected. Extensive straight and level runs (SLRs) in the ash cloud were not permitted owing to stringent exposure limits on the FAAM BAe-146 aircraft.

[29] Figure 4 shows the flight track covered by the FAAM BAe-146 aircraft during the in situ work and a cross section of longitude versus altitude. The DLR Falcon flight track is also shown. This demonstrates that the two aircraft both experienced areas of elevated SO_2, indicative of air of volcanic origin.

[30] Between 14:00 UTC and 16:30 UTC, the FAAM BAe-146 flight comprised the following components used in the analysis presented in this paper:

[31] 1. Straight and level run (SLR) at 7.9 km heading east along 54.0°N. This served to map the ash cloud using the lidar (R2).

[32] 2. Profile descent through the aerosol layer from 7.9 km to 3.0 km, returning west along 54.0°N (P1).

[33] 3. Profile ascent from 3.0 km to 7.6 km near the ash cloud edge heading north. (P2).

[34] 4. SLR at 7.6 km over-flying the ash cloud heading east along 54.5°N (R5).

[35] 5. Profile descent from 7.6 km to 3.0 km through the ash cloud, returning west along 54.5°N (P3).

[36] 6. Profile ascent through the aerosol layer to 6.0 km, (P4), heading southwest.

[37] The goal of the DLR Falcon flight was to intercept and characterize the volcanic ash cloud before it reached northern Germany. The DLR Falcon was not subject to the same operating restrictions as the FAAM BAe-146 and more prolonged exposure to the volcanic ash was permitted. The DLR Falcon work occurred between 15:45 UTC and 17:10 UTC in the area between 52.5 to 53.0°N and 2.0 to 4.5°E (see flight track in Figure 4) and the flight consisted of the following components of interest in this study:

[38] 1. Stacked profile descent from 8.5 km to 2.8 km through the ash cloud, including SLRs at 6.4 km, 6.1 km, 5.8 km, 5.4 km, 4.8 km, 4.2 km and 3.6 km.

[39] 2. Profile ascent from 2.8 km to 8.5 km through the ash cloud heading southeast, interrupted at 4.8 km and 6.0 km for SLRs.

[40] Figure 5 shows the location of in situ measurements made by both aircraft overlaid on satellite imagery from 16:00 UTC. This suggests that both aircraft were effective in targeting the volcanic ash cloud.

[41] Analysis using NAME suggests that the ash cloud the two aircraft encountered was approximately 3 days old. This is in agreement with results presented by *Schumann et al.*

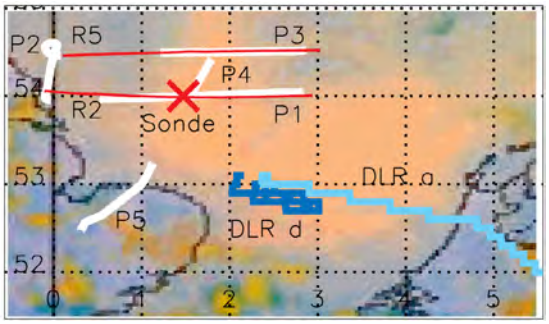

Figure 5. Locations of profiles overlaid on MSG SEVIRI RGB dust product at 16:00 UTC. DLR profiles in blue, FAAM BAe-146 profiles in white, SLRs in red, drop-sonde launch location marked with a red X.

[2011] using FLEXPART and HYSPLIT which yielded 66–82 and 76–88 h respectively. Further confirmation is provided by tracking the ash cloud in SEVIRI imagery.

[42] In order to determine the spatial and temporal coherence of the two data sets, the NAME model was run forward from the time and location of the FAAM BAe-146 profiles, P1 and P3. The results indicate that, although both aircraft were operating in the volcanic ash cloud there is a clear offset in time and space between the two aircraft. Additionally, as has been shown by *Marenco et al.* [2011], the volcanic ash layers were very inhomogeneous exhibiting horizontal and vertical variability even over small distances, further complicating the comparison of the FAAM and DLR data sets. Thus, although any comparison cannot be considered as robust as a wing-tip to wing-tip comparison, given the scarcity of airborne measurements in volcanic aerosol, a comparison of the data from the two aircraft is nonetheless considered worthwhile.

6. Results

6.1. Aerosol Size Distributions

[43] Aerosol number and mass size distributions (Figures 6 (top) and 6 (bottom), respectively) for both aircraft based on assumptions described in sections 3.1 and 4 are given in Figure 6.

[44] The distributions are normalized to the total area under the curve to emphasize the similarity of the shape of the size distributions rather than the absolute magnitude of the number or mass concentrations. Average size distributions from each FAAM BAe-146 profile, P1-P5 are plotted individually alongside that from the DLR Falcon case M average for 16:11:45–16:19:55 UTC, a representative part of the stepped descent. The average for each profile only includes sections where ash was sampled. A bi-modal lognormal fit to the average of all FAAM BAe-146 profiles is also plotted with the geometric mean diameter (D_g), standard deviation (σ) and relative weights in terms of mass (w_M) of the two modes as detailed in Table 2 (FAAM (A)). The lognormal parameters were obtained by fitting manually to capture the peak and width of the observed dM dlogD^{-1} and dN dlogD^{-1} size distributions.

[45] There is relatively little variability in the mass distribution of the coarse mode measured by FAAM BAe-146 on this flight; the peak diameter from different profiles varied between 3.1 μm (P4) and 3.9 μm (P3). The contribution to the mass from the fine mode varies between 2.8% (P3) and 3.8% (P5). Since measurements made by the FAAM BAe-146 are made over a relatively small area and short time period within the same ash cloud, variations due to e.g., aerosol age are expected to be limited. The effect of applying different shape and refractive index assumptions is discussed later in this section.

[46] The mass size distribution derived from DLR Falcon data for case M (Figure 6) is also bi-modal but exhibits a coarse mode with a peak around 10 μm diameter. There are clear differences between the DLR Falcon and FAAM BAe-146 size distributions, in particular at the largest diameters. The coarse mode of the mass size distributions were well approximated by single lognormal fits (see Table 2). The lognormal fit to DLR case M data has a geometric mean diameter of 9.6 μm and standard deviation of 2.5, in contrast with the lognormal fit to FAAM BAe-146 data that has a geometric mean diameter of 3.6 μm and standard deviation of 1.8 (FAAM (A)).

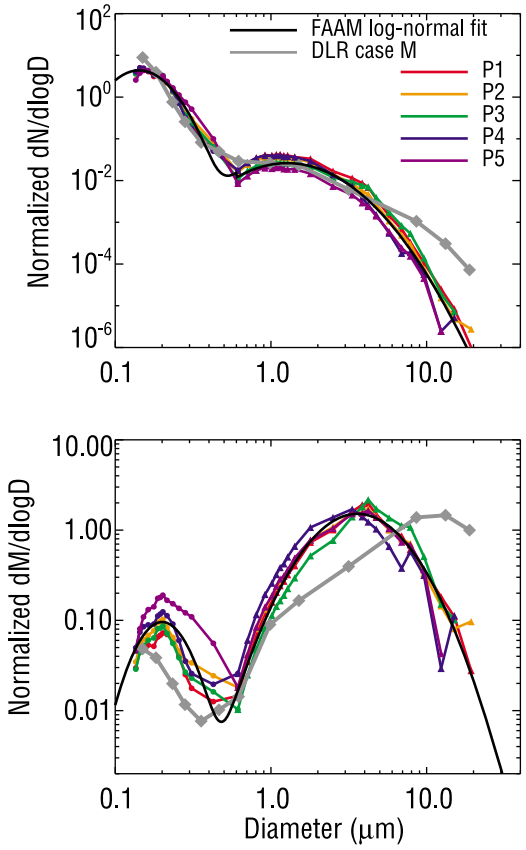

Figure 6. Size distributions of (top) particle number and (bottom) mass concentrations, normalized by the total number and mass concentration respectively for FAAM BAe-146 P1-P5 and for DLR Falcon aircraft case M (16:11:45–16:19:55 UTC). Circles indicate data retrieved from FAAM BAe146 PCASP data, triangles show data from retrieved from CAS. DLR data is shown with diamonds. The black line indicates a lognormal fit to the average dM dlogD^{-1} for P1-P5, transformed to calculate dN dlogD^{-1}.

Table 2. Lognormal Parameters D_g and σ (Geometric Mean Diameter and Standard Deviation, Respectively) and Relative Weight, w_M, Based on the Fit to dM dlogD^{-1} of Average Size Distributions Shown in Figure 7[a]

	FAAM Irregulars (Default) (A)			FAAM Spheres (B)			FAAM, as DLR Case M (C)			DLR Case M (DLR)		
	Fine Mode, Sphere, RI = 1.43 + 0.00i	Coarse Mode, Irregular, RI = 1.52 + 0.0015i	Mean (A)	Fine Mode, Sphere, RI = 1.43 + 0.00i	Coarse Mode, Sphere, RI = 1.52 + 0.0015i	Mean (B)	Fine Mode, Sphere, RI = 1.59 + 0.004i	Coarse Mode, Sphere, RI = 1.59 + 0.004i	Mean (C)	Fine Mode, Sphere, RI = 1.59 + 0.004i	Coarse Mode, Sphere, RI = 1.59 + 0.004i	Mean (DLR)
D_g	0.20	3.6	-	0.20	4.0	-	0.18	4.5	-	0.12	9.6	-
σ	1.4	1.8	-	1.4	1.85	-	1.35	1.9	-	1.6	2.5	-
w_M	0.035	0.965	-	0.028	0.972	-	0.015	0.985	-	0.020	0.980	-
k_{ext}	1.22	0.68	0.70	1.22	0.47	0.48	1.24	0.37	0.38	1.52	0.25	0.27
k_{sca}	1.22	0.65	0.68	1.22	0.44	0.46	1.20	0.32	0.33	1.49	0.21	0.32
f_{ext}	0.07	0.93	-	0.06	0.94	-	0.05	0.95	-	0.07	0.93	-
ω	1.00	0.96	0.96	1.00	0.95	0.95	0.97	0.87	0.88	0.98	0.84	0.85
g	0.43	0.57	0.56	0.43	0.74	0.72	0.35	0.74	0.73	0.34	0.77	0.73
α	3.0	0.0	0.2	3.0	−0.2	0.0	3.3	−0.2	0.0	3.3	−0.3	0.0

[a]Also, the mass specific extinction and scattering coefficients (k_{ext} and k_{sca}), mode extinction fraction (f_{ext}), single scattering albedo (ω), asymmetry parameter (g) at 550 nm and Angstrom exponent (α), derived from the lognormal parameters.

[47] The fine mode measured by the FAAM BAe-146 aircraft during this flight shows similar characteristics to previous observations of accumulation-mode aerosol made with the same instrumentation. The coarse mode is very similar to the mean fit for volcanic ash from all FAAM BAe-146 flights provided by Johnson et al. (submitted manuscript, 2011) that had geometric mean diameter of 3.8 μm and a standard deviation of 1.85. It also shows similarities to observations of Saharan dust [*Osborne and Haywood.*, 2005; *Johnson et al.*, 2008; *Osborne et al.*, 2008]. Johnson et al. (submitted manuscript, 2011) compare the FAAM BAe-146 aircraft size distribution with those derived from AERONET measurements [*Holben et al.*, 1998] made from sites at Helgoland (54.2°N, 7.9°E), Brussels (50.8°N, 4.3°E), and Cabauw (52.0°N, 4.9°E) that sampled the same ash cloud during 17–18 May 2010. Version 2 of the AERONET retrieval algorithm was used to derive size distributions [*Dubovik et al.*, 2006]. The mean mass size distribution for the AERONET sites from Johnson et al. (submitted manuscript, 2011) is shown in Figure 7 alongside the FAAM aircraft mean for this flight and the DLR Falcon case M average for 16:11:45–16:19:55 UTC.

[48] To enable a comparison of the AERONET retrieval with the aircraft data, the amplitude of the AERONET volume distribution has been normalized in the following way. In converting the volume loading to volume concentration, an aerosol layer depth of 1.3 km has been assumed. This is the typical layer depth defined by *Marenco et al.* [2011] in considering lidar measurements as $\sqrt{2}$ × column load/peak concentration. This definition of layer depth is most useful when constructing idealized vertical distributions for use in radiative transfer, or other modeling problems and is applied here to the interpretation of the AERONET retrievals. As has been done for the DLR size distribution, a fine-mode density of 1.8 g cm^{-3} and coarse-mode density of 2.3 g cm^{-3} have been used. Finally, the AERONET dM dlogD^{-1} has been multiplied by a factor of two to approximately match the

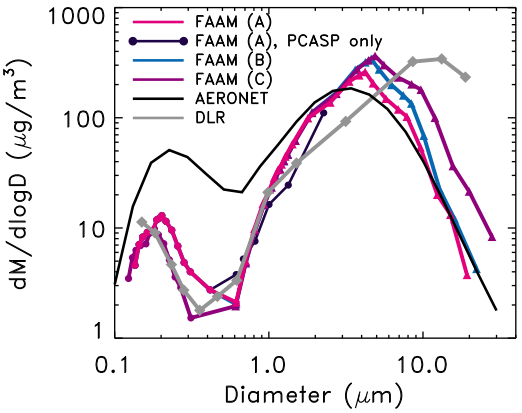

Figure 7. Average mass size distribution from FAAM aircraft assuming coarse mode irregular particles (FAAM A), coarse mode spheres (FAAM B) and the more absorbing DLR case M refractive index and spheres for both the fine and coarse modes (FAAM C). Also shown are the average mass size distributions for DLR case M, AERONET and FAAM PCASP coarse-mode measurements (FAAM density assumptions applied). The AERONET data is multiplied by a factor of two to aid comparison.

amplitude of the coarse mode with the default CAS distribution (irregular shapes). This simply aids the comparison of the coarse-mode peak, width and shape which would be more difficult otherwise. This does not imply a factor of two underestimation between the AERONET and CAS measurements but rather reflects the difficulty of comparing measurements from different locations, given the high degree of spatial variability in column loadings and vertical distributions. The AERONET sites were further south and/or east than the in situ measurements and sampled the ash cloud when it was older and, in the case of Helgoland particularly, nearer the edge of the ash cloud. Therefore a factor of two lower mass concentration seems plausible. The fine mode reported by AERONET is likely to be dominated by boundary layer aerosol. Additionally, although the introduction of spheroids to represent irregular particles in version 2 of AERONET data reduced unrealistically high fine modes exhibited in dust seen in version 1 data, some artificial amplification of the fine mode may still occur since, as shown by *Osborne et al.* [2011], the phase functions of irregular particles are difficult to reproduce with spheroids. For the coarse mode, an encouraging level of consistency is found between the FAAM aircraft in situ measurements derived assuming irregular shapes and the AERONET retrievals. The difference between the size distribution from the AERONET retrieval and that from the DLR Falcon instrumentation is much greater than the difference between the AERONET retrieval and the FAAM BAe-146 (irregular case, FAAM (A)).

[49] The sensitivity of the FAAM aircraft mass size distribution to particle shape and refractive index is demonstrated in Figure 7 together with Table 2. Three versions of the FAAM PCASP and CAS size distribution are presented. FAAM (A) may be considered the default assumptions used throughout this work, as described in section 3.1. FAAM (B) uses the same refractive indices as FAAM (A), but the coarse mode is assumed to consist of spheres rather than irregular shapes. FAAM (C) is derived using the same (more absorbing spheres) refractive indices and spherical shape assumptions as have been used for DLR case M. In all three cases, the standard FAAM densities (1.8 g cm^{-3} and 2.6 g cm^{-3} for the fine and coarse modes respectively) have been assumed.

[50] The effect of assuming spheres rather than irregulars is most pronounced for particles with diameters larger than 3 μm. As demonstrated by Johnson et al. (submitted manuscript, 2011), assuming spheres in the processing of CAS data results in a 20–30% increase of the derived ash mass. The mean diameter for the lognormal fit increases to 4.0 μm and the distribution broadens slightly. Adopting the more absorbing refractive index of 1.59 + 0.004i as well as the spherical assumption, as used in the processing of the DLR Falcon data, led to further amplification of large particles and a 60% increase in mean mass concentrations compared to the default (FAAM A) case. Again, the size distribution broadens slightly and the geometric mean diameter of the lognormal fit increases to 4.5 μm. However, even when FAAM OPC data is processed using the same refractive index and shape assumptions as DLR case M, the mean diameter for the coarse mode is still significantly smaller and the distribution narrower than the DLR case M distribution. For the fine mode, agreement between the DLR and FAAM PCASP instruments is good for diameters larger than 0.18 μm once analysis assumptions are aligned.

[51] Considering the irregular shapes of ash particles shown in SEM images [e.g., *Schumann et al.*, 2011; Johnson et al., submitted manuscript, 2011; T. Navratil et al., Evidence of volcanic ash particulate matter from the 2010 Eyjafjallajökull eruption in dust deposition at Prague-Suchdol, central Europe, submitted to *Journal of Geophysical Research*, 2012], some treatment for the irregularity of particle shapes seems necessary. At present there is not enough information to ascertain whether the roughened polyhedral crystal used here is the most appropriate way of representing the irregularity of the Eyjafjallajökull ash. However, the use of this shape model has improved agreement between modeled and measured radiances for mineral dust [*Osborne et al.*, 2011]. The radiative closure study of *Newman et al.* [2012] shows that the optical properties determined from the CAS size distribution yield broadband and spectrally resolved irradiances in both the solar and terrestrial regions of the spectrum that are consistent with FAAM aircraft radiometric measurements. Additionally, interpreting the coarse mode as irregular shapes yields an improvement over assuming spheres when comparing mass loadings derived from CAS with IASI retrievals [*Newman et al.*, 2012]. These findings further support the assumptions applied in deriving the size distribution from the FAAM aircraft data. The agreement between PCASP and CAS for particle diameters where the two instruments overlap is generally reasonable. This is shown in Figure 7, where PCASP data has been included for the coarse mode assuming spheres with a refractive index of 1.52 + 0.0015i (as for FAAM (B)). This gives some confidence in the performance and interpretation of the CAS and PCASP instruments.

[52] *Johnson and Osborne* [2011] compared coarse-mode size distributions from various dust measurement campaigns. They highlighted the larger coarse-mode volume diameter (10 μm) reported by *Weinzierl et al.* [2009] using two FSSPs on the DLR Falcon when compared to measurements made using the Small Ice Detector (SID-2) or a PCASP-X (measuring up to 5 μm) on the FAAM BAe-146 (3–6 μm). Real differences between the measurements are expected as a result of the different geographic regions sampled and the spatial/temporal variability of dust. More recently, the second Saharan Mineral Dust Experiment (SAMUM-2) used the DLR Falcon to sample transported mineral dust in the Cape Verde region [*Weinzierl et al.*, 2011]. Comparing the SAMUM-2 mass size distribution to that from GERBILS reported by *Johnson and Osborne* [2011] yields a significant improvement in agreement between the coarse-mode measurements from the two aircraft, indicating that differences between SAMUM-1 and GERBILS mass size distributions are probably due in large part to the age of the dust. Radiative closure studies such as those of *Haywood et al.* [2011] and *Osborne et al.* [2011] for dust sampled during the GERBILS project, *Newman et al.* [2012] for volcanic ash and *Otto et al.* [2009] for SAMUM dust measurements, demonstrate that the measured size distributions can be used in radiative transfer calculations to successfully model simultaneous radiative measurements. A lab intercomparison study and/or wingtip-to-wingtip comparison flight would be invaluable to

determine the extent that instrumental issues may contribute rather than atmospheric variability.

6.2. Volcanic Aerosol Optical Properties

[53] The extinction and scattering of radiation due to each mode in the size distribution may be calculated using the lognormal fits to the size distributions shown in Figure 7, detailed in Table 2. The mass specific scattering coefficient (k_{sca}) at an appropriate wavelength in particular is important in estimating total aerosol mass from the scattering coefficient and vice versa via equation (1), thereby allowing a comparison of OPC and nephelometer data. Since the nephelometer is an integrating measurement, it is not possible to consider purely the coarse mode, attributed to volcanic ash, so an average k_{sca} for both modes is used in applying equation (1). However, extinction, and therefore scattering, at 550 nm is heavily dominated by coarse-mode particles (diameters between 0.8 μm and 7 μm, f_{ext} in Table 2). The mass specific extinction coefficient (k_{ext}) is required in the derivation of mass concentration estimates from lidar and passive remote sensing data such as from Sun photometers and satellites.

[54] The specific scattering and extinction coefficients (k_{sca} and k_{ext}), single scattering albedo (ω), asymmetry factor (g) (all at 550 nm) and Ångström exponent between 700 nm and 450 nm (α) derived from lognormal fits to the distributions in Figure 7 are detailed in Table 2. Optical parameters based on the three different derivations of the FAAM OPC size distribution are presented; the default case as presented in section 3.1 (FAAM (A)), assuming the default refractive indices but applying spheres rather than irregulars to the coarse mode (FAAM (B)) and applying the more absorbing spheres used as the basis for DLR Falcon case M (FAAM (C)).

[55] At a wavelength of 550 nm, k_{sca} derived for the fine-mode particles is estimated to be 1.22 $m^2\ g^{-1}$, while for the coarse-mode particles it is estimated to be 0.65 $m^2\ g^{-1}$. The much reduced k_{sca} for coarse-mode particles is typical of particles such as Saharan dust [e.g., *Osborne et al.*, 2008]. A value of k_{sca} of 0.68 $m^2\ g^{-1}$ (weighted average of k_{sca} for the individual modes) will be used in this paper to estimate the volcanic ash mass concentration from the nephelometer scattering coefficient. The dependence of optical parameters on mass concentration, respectively effective diameter, has been discussed by *Schumann et al.* [2011].

[56] As was evident in Figure 7, assuming spheres rather than irregulars (comparing FAAM A and FAAM B) increases the mean diameter and broadens the distribution. The effect on the optical properties is to reduce the coarse-mode mass specific extinction and scattering by approximately 30% while slightly increasing the coarse-mode extinction fraction (f_{ext}) and making the asymmetry factor, g, larger. Applying the DLR case M assumptions to the FAAM OPC data (comparing FAAM C and FAAM B) decreases the mass specific extinction and scattering by a further 20% and decreases ω by 10%, as is expected given the increased absorption and mass. However, the mass specific extinction is still larger than that derived from the lognormal fit to the DLR Falcon case M size distribution, a consequence of the smaller mean diameter.

[57] Since the DLR case M coarse mode is shifted to larger sizes relative to the FAAM BAe-146 average, the mass specific extinction (0.25 $m^2\ g^{-1}$) is correspondingly lower, and the asymmetry factor, g, is significantly larger. The degree of absorption arising from the imaginary part of the complex refractive index leads to differences between k_{ext}, k_{sca} and ω derived from FAAM BAe-146 and DLR data. Assuming spheres rather than irregular shapes for the coarse mode also affects the derived k_{ext} and k_{sca} as well as the asymmetry parameter, g. However, as was shown in section 6.1 and Figure 7, differences between the DLR and FAAM size distributions and therefore the optical parameters derived from them cannot be attributed entirely to assumptions made in data processing. It is likely that variations in instrument performance also contribute to variation in the derived optical parameters.

6.3. Time Series of Ash Cloud Penetrations

[58] Figure 8 shows time series of the in situ measurements made by the FAAM aircraft during the 17 May 2010 flight.

[59] The ash mass derived from CAS and from the nephelometer are shown in Figure 8a, along with the aircraft altitude. Areas shaded in gray indicate where volcanic ash was sampled. A discussion of how aerosol mass derived from CAS and the nephelometer compares can be found in section 6.5. Five profiles (P1-P5) through the volcanic ash aerosol layer stand out as displaying significant ash mass concentrations (>100 μg m^{-3}). The locations of these profiles relative to the ash cloud are indicated in Figure 5, although it should be noted that the underlying satellite picture is valid at 16:00 UTC while profiles occurred between 14:40 and 16:50 UTC. The highest mass concentrations were encountered during P1 where peak ash concentrations reached around 500 μg m^{-3}. If spheres with the same refractive index rather than irregulars are assumed (FAAM B), this peak ash concentration increases by 25% to $\sim$630 μg m^{-3}. The result of applying the more absorbing case, FAAM C, is to increase the peak ash concentration by a further 25% to $\sim$780 μg m^{-3}. However, FAAM A constitutes the best estimate of peak ash concentration on the FAAM BAe-146 flight and carries an uncertainty of a factor of 2, which encompasses the other two FAAM cases.

[60] The aerosol scattering measured by the nephelometer at three wavelengths is shown in Figure 8b. During all the ash cloud encounters on this flight, the signal at 700 nm is larger than that at 450 nm. The Ångström exponent, α, calculated from the nephelometer measurements between 450 and 700 nm is also shown in Figure 8b and is indicative of the spread between the wavelengths which is related to the size of the particles. In the aerosol layer, α is approximately -0.3, indicating a small sensitivity of scattering to wavelength due to the dominance of large particles in the sample. The observed value of α is low compared to the calculated values of 0.2 and 0.0 given in Table 2 that were based on the measured size distribution assuming irregulars and spheres respectively for the coarse mode. The observed value of α is also a little lower than values of 0.0 ± 0.2 measured in Saharan dust by *Johnson and Osborne* [2011] during the GERBILS project and values between -0.20 and +0.04 reported by *Osborne et al.* [2008] on the Dust and Biomass-burning Experiment. However, there is no apparent evidence for instrumental bias in either of the nephelometer channels used. The combination of elevated aerosol mass coupled with low α gives confidence that the aerosol

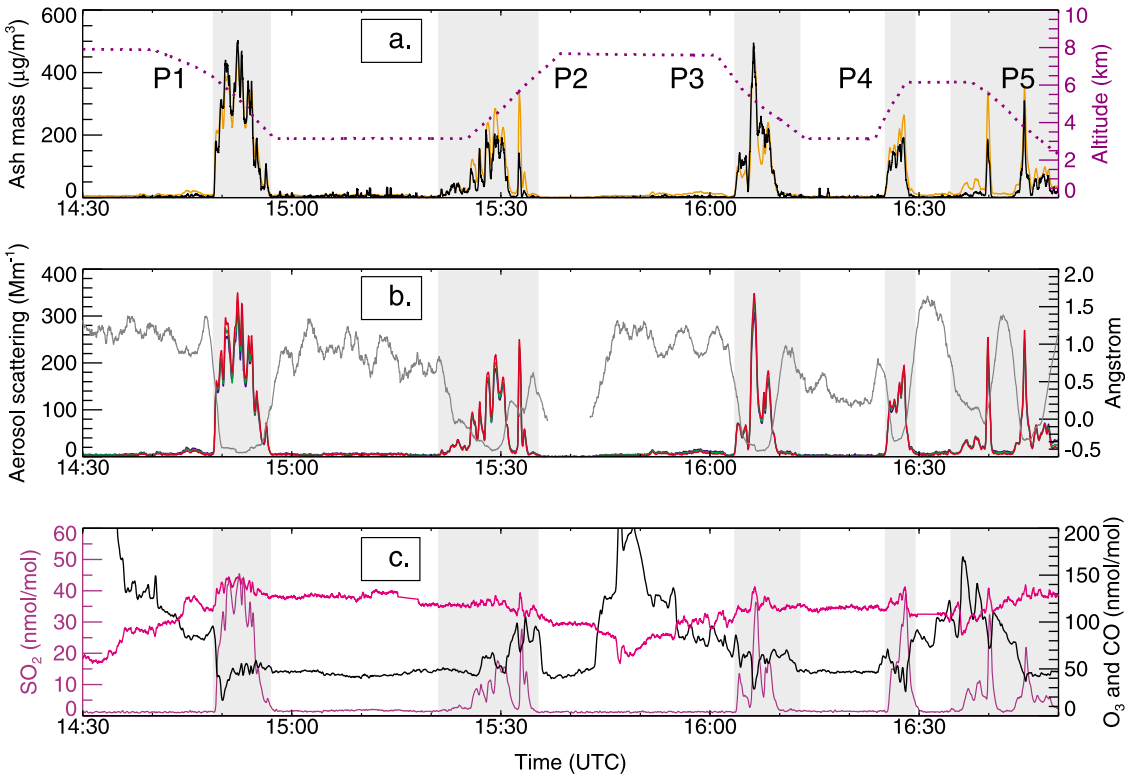

Figure 8. Time series of a selection of FAAM BAe-146 in situ measurements. (a) Ash mass from CAS (black) using the default FAAM A assumptions and derived from the nephelometer (orange), aircraft altitude (purple). (b) Nephelometer scattering at 450 nm (blue), 550 nm (green) and 700 nm (red) and Angstrom exponent (gray, right hand axis). (c) SO_2 (purple), O_3 (black) and CO (pinkish-red). Periods when volcanic aerosol was sampled are highlighted by gray shading.

sampled on each of the five profiles was dominated by coarse volcanic ash particles, as has already been demonstrated by the size distribution (section 6.1).

[61] Figure 8c shows SO_2, O_3 and CO measurements. Volcanoes are a significant source of atmospheric SO_2 [*Hobbs et al.*, 1991; *Hunton et al.*, 2005; *Carn et al.*, 2011]. During periods where elevated aerosol mass and low α are encountered, concurrent increases in SO_2 are also observed [see also *Schumann et al.*, 2011]. The relative peak sizes between the five profiles are similar to those observed in both the ash mass concentration and scattering signals. In this study where only a small geographic area is sampled in detail, SO_2 is co-located with the volcanic aerosol. However, the satellite study of *Thomas and Prata* [2011] suggested that over larger spatial scales, ash and SO_2 are not necessarily co-located.

[62] Owing to the variable vertical structure of O_3 and the presence of high levels of O_3 above the ash cloud induced by a tropopause fold, it is difficult to establish a background O_3 level on this day. It is expected that O_3 will be destroyed by reactive halogens emitted by the volcano and CO is enhanced in the ash cloud [e.g., *Rose et al.*, 2006]. Although the detail is blurred by the relative response times of the O_3, SO_2 and CO instruments, O_3 appears to be depleted by approximately 30 nmol mol^{-1} in the ash cloud while CO is elevated by approximately 20 nmol mol^{-1}. This is in agreement with modeling work by both *von Glasow* [2010] and *Roberts et al.* [2009] and has been discussed recently by *Vance et al.* [2010].

[63] The combination of OPC derived aerosol mass, nephelometer scattering and α coupled to SO_2 measurements, lidar depolarization (not shown here), satellite detection algorithms and plume dispersion modeling, provides clear and coherent evidence that volcanic ash was sampled on each of the five profiles.

[64] The time series of data collected by the DLR Falcon are shown in Figure 9. Figure 9 (top) shows the total aerosol mass [*Schumann et al.*, 2011], case M density adjusted) and the aircraft altitude. The peak total aerosol mass sampled was 540 $\mu g\ m^{-3}$; w_M of 0.98 (Table 2) for the coarse mode suggests that ~530 $\mu g\ m^{-3}$ of this was ash. In Figure 9 (bottom) measurements from the SO_2, O_3 and CO instruments are shown, exhibiting similar characteristics to those seen in Figure 8c. SO_2 appears to be correlated with the aerosol mass while O_3 is depleted within the ash cloud and CO is elevated. These measurements confirm that the DLR Falcon was sampling volcanic ash cloud of very similar characteristics to the FAAM aircraft.

[65] Since the DLR Falcon measurements were made further south than those from the FAAM BAe-146 (Figure 5), the ash sampled by the DLR Falcon must be older. NAME trajectories (not shown), suggest that FAAM BAe-146 profiles are approximately 1.25 h (P1) to 3.5 h (P3) upwind of the DLR aircraft and that P3 was directly upwind

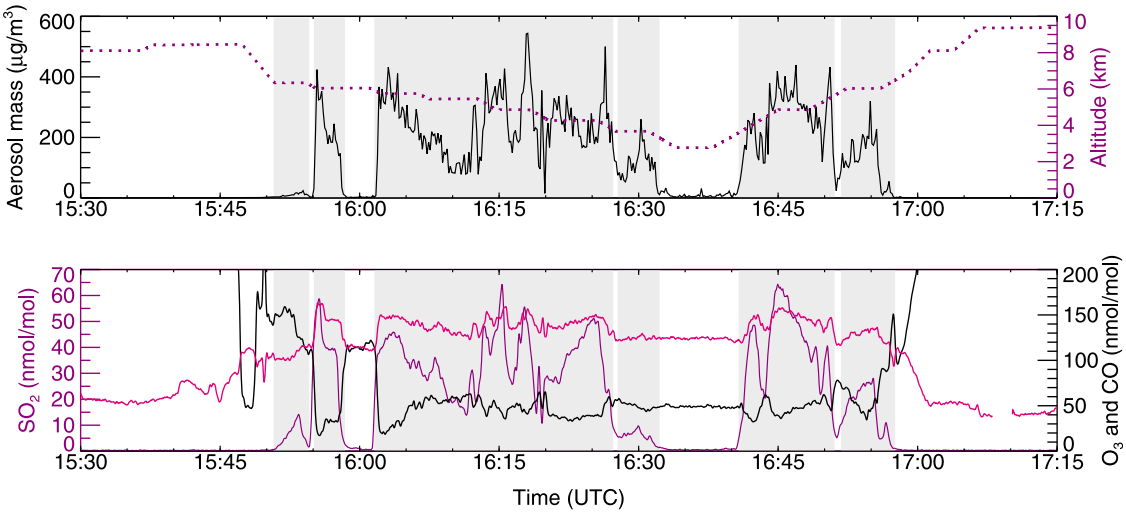

Figure 9. Time series of DLR in situ measurements over southern North Sea. (top) Aerosol mass concentration and aircraft altitude. (bottom) SO_2, O_3, CO (colors as used in Figure 8).

of the area where DLR performed its stepped descent. Thus while the comparison cannot be categorized as a robust wing-tip to wing-tip calibration validation, the general agreement in terms of the absolute magnitude of the aerosol mass and gas phase concentrations gives confidence that the instrumentation on both aircraft was fully functioning.

6.4. Vertical Distribution and Variability of Ash Layers

[66] As shown in Figure 5, P2 and P5 sampled areas with lower quantities of ash. P1, P3, P4 and the descent and ascent stepped profiles from DLR all sampled areas that appear qualitatively similar on the satellite image (brighter orange). P5 exhibited a noticeably different vertical structure with two distinct narrow layers, in contrast to the single deep layers sampled on P1-P4. Since sampling very thin layers is problematic owing to differences in the response of individual instruments, P5 is overlooked in discussions of profiles. Figure 10 comprises in situ data from a selection of vertical profiles through the volcanic ash cloud.

[67] In Figure 10a, FAAM BAe-146 P1 data is shown. Ash mass from the OPCs is plotted alongside the concentration of SO_2 (top axis). Figure 10b shows the two DLR stepped profiles as 300 m median values, as used by *Schumann et al.* [2011]. Aerosol mass for case M, their best estimate, is plotted alongside concentrations of SO_2. Solid lines are used for descent data and dashed lines for ascent data.

[68] The top of the ash cloud was encountered at 6.1–6.5 km in all cases (including the profiles not shown), while the base varied between 3.3 km and 4.2 km. The base of the layer was lower in the west and south of the measurement area (P1, P2, P5 and DLR) while the higher base (P3, P4) corresponded to measurements made in the northeast. *Marenco et al.* [2011] define a typical layer depth as $\sqrt{2}$ × column load/peak concentration as a useful constraint

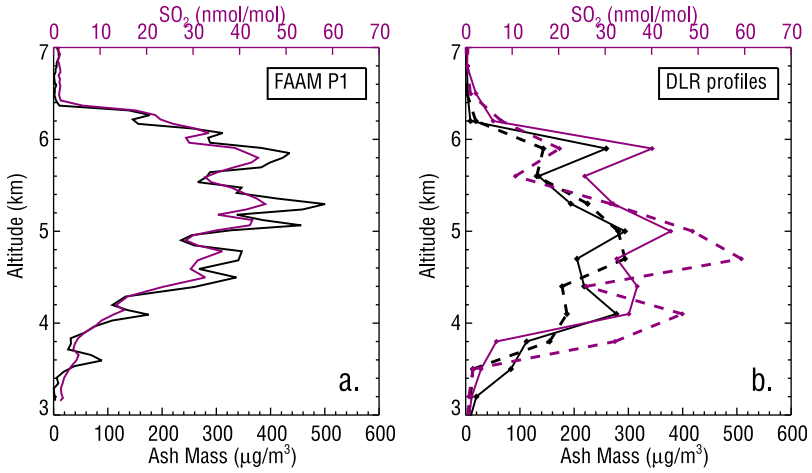

Figure 10. Profiles from (a) FAAM BAe-146 P1 using default (FAAM A) processing and (b) DLR descent (solid lines) and ascent (dashed). Aerosol coarse-mode mass from OPCs is in black, SO_2 is purple (top axis). DLR data are 300 m median values.

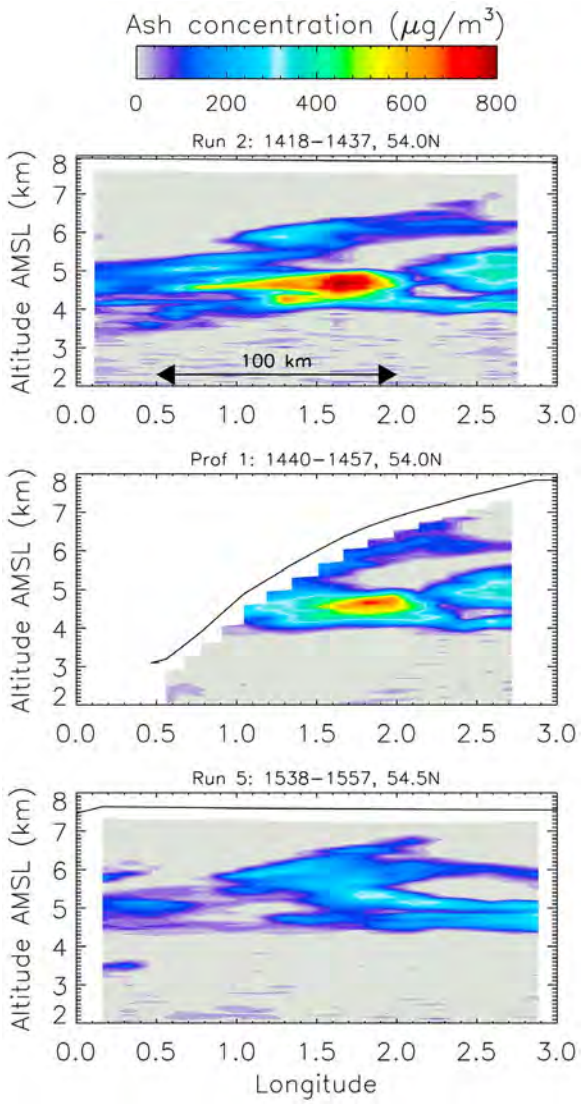

Figure 11. FAAM BAe-146 lidar ash mass (μg m^{-3}) longitudinal cross sections. (top) Run R2. (middle) Profile P1 (both 54.0 N). (bottom) Run R5 (54.5 N). At these latitudes, 1.5° longitude equates to ~100 km.

when approximating observed profiles with idealized vertical distributions. Using the same definition for in situ profile data yields typical layer depths ranging from 1.0 to 2.0 km. Within the 2.0–2.5 km overall altitude range of the ash cloud, there is significant variability in the vertical. The structure within the ash cloud varies markedly between P1 and P3 (Figure 8), while there are clear similarities between P1 and the DLR descent profile. Aerosol mass concentration cross sections derived from the lidar on the FAAM BAE-146 aircraft are shown in Figure 11 and confirm these observations.

[69] Figure 11 depicts the ash concentration derived from the lidar in the form of a longitude/height cross section for runs R2 and R5 and for profile P1. The lidar observed the ash layer between 3.5 km and 7.0 km altitude, with a west-east positive slope and developing into a double layer toward the eastern side. The along-track dimension of the region of maximum concentration (>500 μg m^{-3}) was approximately 85 km in the horizontal. This again emphasizes the spatial inhomogeneity of the ash cloud in both the horizontal and vertical. For example, Figure 11 shows that the lidar mass concentrations vary between around 800 μg m^{-3} at 4.5 km altitude, 54°N 1.7°E, but fall to below 50 μg m^{-3} at 2.1°E, a distance of only 25 km.

[70] An aircraft profile through the ash cloud would only have to be displaced by as little as 0.5° (35 km at these latitudes) in either direction to yield markedly different ash exposure. This extreme inhomogeneity highlights just how difficult it is to target (or conversely avoid) the most dense ash patches with aircraft and to definitively model atmospheric concentrations in space and time with numerical models such as NAME.

6.5. Correlations

[71] Figure 10 confirms that there is a high degree of correlation between the plotted parameters, as was previously suggested for a wider range of measurements in Figures 8 and 9. Scatterplots comparing aerosol scattering coefficient, ash mass and SO_2 concentration are presented in Figure 12, with data from each profile highlighted in different colors.

[72] Given perfect instrumentation, the regression slope of aerosol scattering coefficient and ash mass (Figure 12a) would be equal to $k_{sca}\ w_M(c)^{-1}$ (equations (1) and (2), dashed line in Figure 12a) making the ash mass estimated from the nephelometer equivalent to ash mass derived from the OPC. The correlation can only be ideal when the shape of the particle size distribution and hence the effective diameter, k_{sca} and $w_M(c)$ are constant. Using an average k_{sca} and $w_M(c)$ results in an additional source of systematic deviations. Table 3 lists the Pearson correlation coefficients and linear fit parameters derived using a least squares absolute deviation method (plotted as solid lines in Figure 12).

[73] Although the correlations in each case are strong, the slope is up to 12% lower than the CAS derived k_{sca} during descents (P1 and P3) and up to 22% higher for ascents (P2 and P4). Similar problems have been highlighted before; *Haywood et al.* [2003] showed that the same PCASP installed on the C-130 aircraft was sensitive to the angle of attack of the aircraft during a stacked profile descent through a thick layer of biomass burning smoke. *Haywood et al.* [2003] found that higher concentrations were measured by the PCASP while performing profile descents (aircraft pitch ~3.4°) than during SLRs (aircraft pitch 4.8°). The evidence here suggests that the CAS tends to measure less mass when the aircraft is in profile ascent than in profile descent, although the size distribution is almost identical between ascents and descents (Figure 6). However, taking the average of the slopes over two ascents and two descents results in $k_{sca}\ w_M(c)^{-1} = 0.73$ m^2 g^{-1}. Applying $w_M(c) = 0.965$ (Table 2), yields k_{sca} estimated via this method of 0.70 m^2 g^{-1}, indicating that the average mass derived from the nephelometer is on average within 5% of the CAS estimates. Given that the nephelometer is served by a Rosemount inlet whose sampling efficiency as a function of aerosol size is not well understood, the agreement between the two instruments is surprising but well within uncertainties associated with each measurement. One explanation for the agreement could be that the loss of the largest particles is compensated for by enhancing the number concentration of

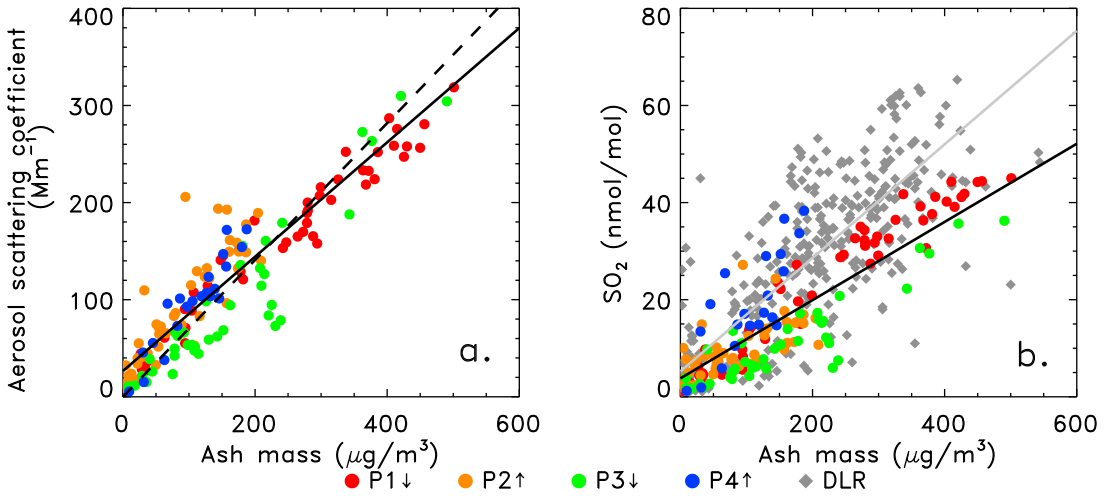

Figure 12. Scatterplots of (a) aerosol scattering coefficients and ash mass concentration and (b) SO_2 concentration and ash mass. Ten second averages are used. Solid lines are linear fits to data, black for FAAM, gray for DLR data. Dashed line indicates expected relationship between aerosol scattering and ash mass.

smaller coarse-mode particles. So, for instance, if particles with diameter >4 μm were not sampled, the loss of signal could be compensated by enhancements of coarse-mode particles with diameters <4 μm. However, this is merely speculation and characterization work is essential to fully understand the inlet before firm conclusions may be drawn.

[74] Figure 12b highlights a strong correlation between SO_2 concentration and aerosol mass for each profile on this flight but with significant variations in the relationship. *Schumann et al.* [2011] report that for this specific volcano and the eruption in April/May 2010, an ash concentration of 1 mg m^{-3} corresponds to about 170 nmol mol^{-1} SO_2 enhancement in mixing ratio. On the day of this case study, DLR measurements (black diamonds) yield approximately 120 nmol mol^{-1} SO_2 enhancement for 1 mg m^{-3} ash, while measurements from the FAAM BAe-146 vary between 60 nmol mol^{-1} (P2) and 210 nmol mol^{-1} (P4) for 1 mg m^{-3} ash, with an average of around 110 nmol mol^{-1} per mg m^{-3}. In this particular case, SO_2 concentration proves to be a reliable tracer for the Eyjafjallajökull ash cloud. However, SO_2 and ash do not necessarily follow the same trajectory and will be subject to very different wet deposition removal processes, as found in the study by *Thomas and Prata* [2011].

6.6. Comparing FAAM BAe-146 and DLR Falcon Data

[75] Similarities between FAAM BAe-146 P1 and the DLR ascent are demonstrated most clearly in Figure 13. Profiles of aerosol mass concentration (Figure 13, top left), SO_2 (Figure 13, top right), O_3 (Figure 13, bottom left) and CO (Figure 13, bottom right) for FAAM BAe-146 P1, P3, P4, DLR descent and ascent (300 m medians) are directly compared. Only P1, P3 and P4 are shown in this section as they are in the area of the ash cloud expected to be upwind of the DLR Falcon sampling area (Figure 5), whereas P2 and P5 are further west.

[76] The gas phase chemical composition within the ash cloud as measured by DLR is most like that observed during FAAM BAe-146 P1, with comparable concentrations of SO_2, O_3 and CO. It might be expected that the mass from P1 should therefore also compare most favorably with DLR Falcon profiles. While the depth of the layer and the structure is similar, the mass retrieved from the DLR Falcon data is approximately 40% lower than FAAM data when the default assumptions are applied. Once particle property assumptions are unified (FAAM (C)), the FAAM aircraft CAS mass concentrations become a factor of 2.5 larger than those from the Falcon FSSP. Given that the optical scattering collection angles (4–12°) and working principals of the CAS and FSSP instruments are essentially identical, this factor of 2.5 difference must arise either from spatial and/or temporal variability of the ash clouds or other instrumental uncertainties.

Table 3. Correlations Between Aerosol Mass Concentration, Scattering and SO_2

Nephelometer Scattering Versus CAS Mass (Figure 12a)	Slope (m^2 g^{-1})	Pearson r^2	Number of Points Included
P1	0.61	0.98	51
P2	0.86	0.88	49
P3	0.62	0.94	39
P4	0.83	0.94	21
P1-P4 ave	0.73	-	-
Nephelometer-Derived Mass Versus CAS Mass	**Slope**	**Pearson r^2**	**Number of Points Included**
P1	0.88	0.98	51
P2	1.22	0.84	49
P3	0.93	0.93	39
P4	1.09	0.92	21
P1-P4 ave	1.03	-	-
SO_2 Versus CAS Mass (Figure 12b)	**Slope (nmol mol^{-1} (mg m^{-3})$^{-1}$)**	**Pearson r^2**	**Number of Points Included**
P1	98	0.97	51
P2	58	0.64	49
P3	75	0.91	39
P4	214	0.74	21
P1-P4 ave	111	-	
DLR	117	0.75	316

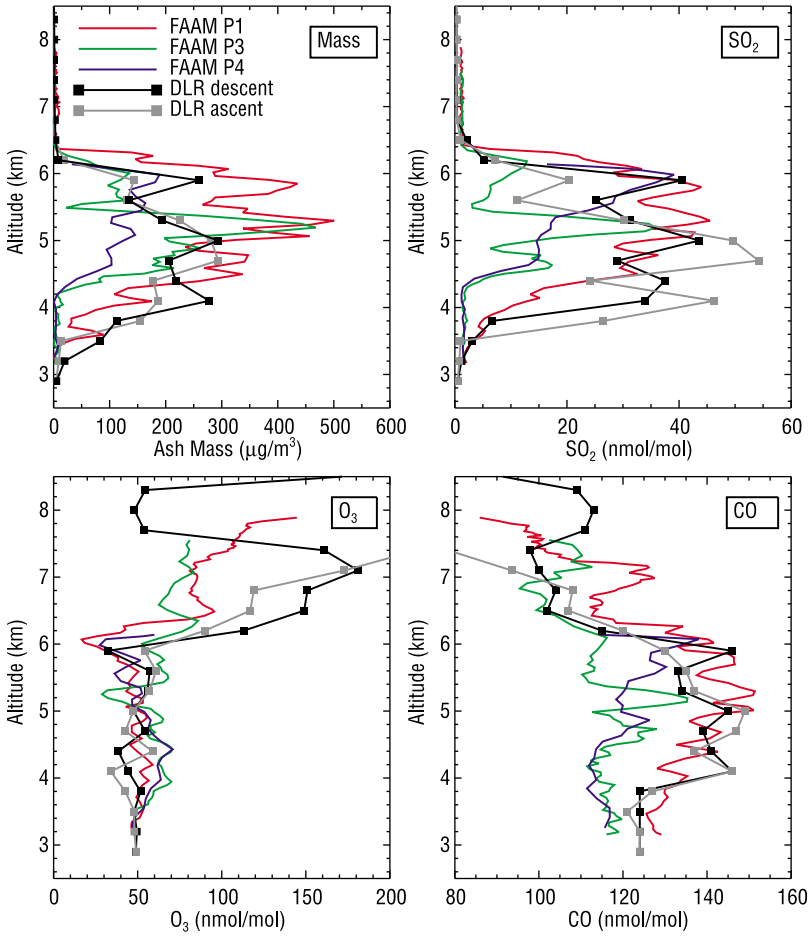

Figure 13. Profiles of (top left) ash mass, (top right) SO_2, (bottom left) O_3 and (bottom right) CO from FAAM BAe-146 aircraft P1, P3 and P4, and DLR ascent and descent stepped profiles.

The latter could include uncertainties in sample and volume particle size calibration, or variations in the performance of the optics and electronics between the instruments. Refractive index and shape assumptions alone cannot reconcile the difference.

6.7. AOD and Column Mass Loadings

[77] Using k_{sca} and $w_M(c)$ to convert between aerosol mass and scattering coefficient (equations (1) and (2) and Table 2), allows aerosol optical depth (AOD) and column mass loading for the aerosol layer to be derived using both the nephelometer and OPCs for each FAAM BAe-146 profile. The results are summarized in Table 4.

[78] The atmospheric optical depth at 550 nm (AOD) and column mass loading of the ash layer calculated from the two instruments compare favorably, which is expected given the reasonable optical closure obtained in the previous section. The largest AOD and column mass loading was sampled on P1, where the AOD and mass loading were 0.5 and 0.7 g m^{-2} respectively and the peak mass concentration

Table 4. Comparison of AOD and Column Mass Loading of Volcanic Ash Layer and Peak Ash Mass Concentration Derived From CAS and Nephelometer for Each FAAM BAe-146 Profile[a]

	AOD		Column Ash Loading (g m^{-2})		Peak Ash Concentration (μg m^{-3})		Peak SO_2 (nmol mol^{-1})	SO_2 Column (Dobson Units)
	OPCs	Neph	OPCs	Neph	OPCs	Neph		
P1	0.48	0.49	0.71	0.72	500	470	46	4.5
P2	0.15	0.23	0.22	0.33	220	330	29	1.7
P3	0.23	0.20	0.34	0.30	500	470	37	1.5
P4	0.15	0.20	0.22	0.29	190	260	40	1.8
Mean	0.25	0.28	0.37	0.41	350	380	38	2.3
Standard deviation	0.16	0.14	0.23	0.20	170	100	7	1.5

[a]The k_{sca} = 0.68 m^2 g^{-1} value is used to convert between mass and scattering. Mean values exclude P5.

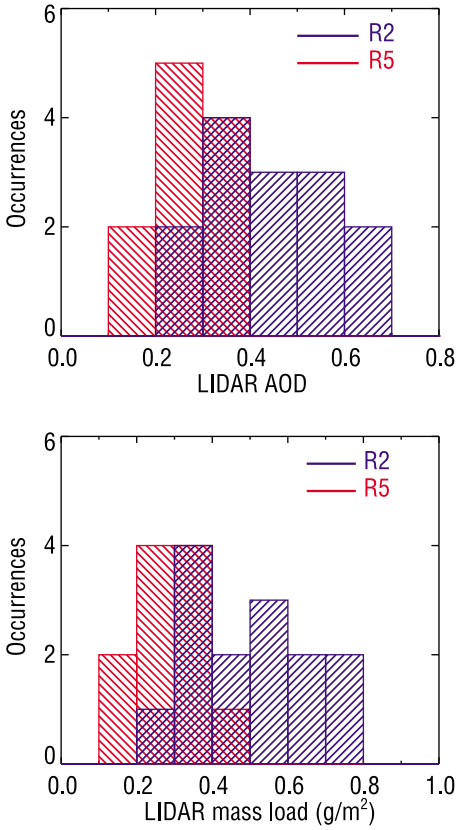

Figure 14. Probability distribution functions of (top) AOD and (bottom) mass loading derived from the 1-min (~8–10 km) integrated lidar data.

was 500 μg m^{-3}. The average AOD was 0.25 with a standard deviation of 0.16, equivalent to an average column mass load of 0.37 g m^{-2} with a standard deviation of 0.23 g m^{-2}.

[79] Lidar profiles will always be offset from in situ profiles in either space and/or time when using a single aircraft for both in situ and lidar measurements. *Marenco et al.* [2011] investigate in detail the column loadings and volcanic ash mass concentrations inferred from the lidar during all of the FAAM BAe-146 flights performed during the Eyjafjallajökull eruption. On the flight discussed here, two aircraft profiles doubled back under high level SLRs, sampling air that had recently been characterized by the lidar. Comparing the AOD calculated from in situ measurements with any single lidar profile is not meaningful owing to the extreme spatial inhomogeneity evident in the ash cloud (section 6.4) and the considerable horizontal distance traveled by the aircraft during a profile. Instead, it is useful to calculate a probability distribution function from the lidar profiles over the longitude range covered by the in situ profile through the ash cloud. This gives information on the spatial variation in the ash cloud and the range of AODs or column mass load that would be expected. One-minute integrated lidar profiles were used to yield the probability distribution functions for both AOD and column loading shown in Figure 14. There are 14 1-min integrated lidar profiles suitable for the comparison from R2 while for R5, there are 11.

[80] In order to calculate the column mass loading from the lidar, k_{ext} and coarse extinction fraction calculated from the PCASP and CAS size distribution at the lidar wavelength (355 nm) were applied. Comparing Figure 14 with the values detailed in Table 4 (R2 with P1, R5 with P3) reveals that the in situ measurements fall within the expected range of values for both AOD and column mass load as derived from the lidar. The data shown in Figure 14 is comprised of data with a 1 min integration time which corresponds to a footprint of approximately 9 km. For R2, the lidar-derived aerosol column loading varied from around 0.2–0.8 g m^{-2} highlighting the large variability of the ash layer. In this instance, over a distance of around 100 km the column loading varied by a factor of three.

[81] AERONET sites are too far from the aircraft measurements for rigorous validation and, additionally, capture boundary layer aerosol that is excluded from both the aircraft in situ and lidar AOD estimates. AODs at 440–675 nm at the three AERONET sites rose to between 0.4 and 0.5 as the ash cloud passed over their locations late on 17 May 2010 and early on 18 May 2010 and the coarse-mode AOD/fine-mode AOD increased significantly.

[82] Table 5 compares AOD, column mass loadings, peak mass and SO_2 concentrations from the in situ and lidar retrievals from FAAM BAe-146, and the DLR Falcon in situ measurements.

[83] The highest derived mass of approximately 800 μg m^{-3} was that obtained by the lidar. This is reasonable since the lidar is capable of mapping out the AODs, column burdens, and atmospheric concentrations throughout the atmosphere, while aircraft making in situ observations are unlikely to fly through the areas with the highest concentrations (see Figure 11 (middle), in particular the position of the region of highest concentrations relative to the aircraft track during P1). Most of the work presented here occurred in a small area where NAME indicated peak ash concentrations below 200 μg m^{-3}. Comparing the locations of the observations (Figure 5) with model output (Figure 2) suggests that the westward extent of the ash cloud over the North Sea was not captured fully by the NAME model. The forecast ash

Table 5. Comparison of AOD and Column Loading for the Aerosol Layer, Maximum Ash and SO_2 Concentrations Observed by DLR, FAAM BAe-146 in Situ Measurements (Excluding P5, out of Main Plume) and the FAAM BAe-146 Lidar

	Aerosol Optical Depth	Ash Column Loading (g m^{-2})	Peak Ash Mass (μg m^{-3})	SO_2 Peak (nmol mol^{-1})	SO_2 (DU)
DLR	0.15	0.6	540	70	4.2
FAAM in situ (P1-P4)	0.15–0.5	0.2–0.7	500	50	1.5–4.5
FAAM lidar R2 (P1)	0.2–0.7	0.2–0.8	800	-	-
FAAM lidar R5 (P3)	0.1–0.4	0.2–0.5	340	-	-
FAAM lidar all ash cloud area	0.1–0.7	0.1–0.8	800	-	-
All	0.1–0.7	0.1–0.8	800	70	4.5

over land areas of the UK was not detected in the FAAM aircraft lidar measurements. This highlights the difficulties in forecasting such events and demonstrating the importance of high quality in situ and remote sensing validation data from observational platforms such as the FAAM BAe-146 and DLR Falcon. *Webster et al.* [2012] compare a range of in situ and remote observations, including those from the aircraft on this flight, with NAME modeled concentrations for the Eyjafjallajökull event as a whole.

7. Conclusions

[84] This study documents in situ measurements from a flight made by the FAAM BAe-146 aircraft that encountered volcanic ash from the eruption of Eyjafjallajökull. It also presents a comparison of these measurements with those made nearby on the same day by the DLR Falcon [*Schumann et al.*, 2011]. The observations show an ash cloud over the southern North Sea between altitudes of 3.5 and 6.5 km. Both data sets show similar vertical distributions, similar elevations of SO_2 concentration, and similar magnitudes of ash mass when processed with their own independent particle property assumptions. This agreement, despite the absence of wing-tip to wing-tip flight co-ordination, indicates that both aircraft sampled similar ash clouds.

[85] Within the ash cloud, the concentrations of aerosol mass and trace gases were highly variable in both the vertical and horizontal. In situ measurements showed variations in mass concentration from $\sim$50 μg m^{-3} to peak values of 500 μg m^{-3} across altitude ranges as little as 300 m. The lidar showed mass concentrations varying in the horizontal from $\sim$50 μg m^{-3} to peak values of 800 μg m^{-3} on length scales as small as 25 km. These extreme variations in the aerosol mass loading demonstrate the difficulties in devising practical ash avoidance procedures for civil aircraft; small changes in altitude (a few hundred meters) or geographic position (a few tens of km, equivalent to a few minutes of flight time) may result in an aircraft being exposed to ash concentrations that change by a factor of more than 10.

[86] When the Falcon and FAAM aircraft data were processed with their own independent particle property assumptions the aerosol mass derived from DLR Falcon profiles was approximately 40% lower than that from the FAAM aircraft on profiles with similar vertical structure and comparable SO_2, O_3 and CO concentrations. This difference would be well within the factor of two uncertainty that is deemed appropriate for both FAAM BAe-146 and DLR Falcon estimates of mass concentration data arising from uncertainties in the assumptions regarding particle composition, shape and density, and inherent uncertainties in optical particle counting techniques [*Schumann et al.*, 2011; Johnson et al., submitted manuscript, 2011]. However, when particle property assumptions were unified by adopting the spherical shape assumption and refractive index used in the DLR Falcon case M data processing, the FAAM-derived ash mass was a factor of 2.5 higher than the DLR-derived mass. The spatial variability of the ash cloud may be a large contributor to this difference as the two sets of measurements were displaced in time and space by approximately 170–240 km and 1.25–3.5 h. The large difference in mass, despite similar concentrations and vertical profiles of SO_2, CO and O_3, indicates a need for more stringent intercomparisons of optical particle counters and characterization of their response to ash aerosol. Wingtip-to-wingtip measurements in future campaigns investigating coarse aerosol would be very beneficial, in particular during a future volcanic ash episode.

[87] The aerosol mass size distribution calculated from PCASP and CAS on the FAAM BAe-146 peaked at diameters of 0.2 μm and 3.6 μm for the fine and coarse modes respectively. The maximum diameter of ash (defined here as the upper bound of the CAS bin the largest particle occurred in) encountered on this flight was 23 μm. The result of assuming spheres (FAAM B) is to increase the maximum diameter to 28 μm and for the more absorbing spheres of FAAM C, the maximum diameter becomes 36 μm. Since FAAM C is considered to be the extreme case, it forms the upper limit of the estimated maximum diameter of the ash. Although this may seem a large increase in diameter (60%), it should be remembered that particles in the largest bin do not contribute very much to the overall mass owing to their low number concentrations. The AERONET mass size distribution derived from surface based measurements appears to agree with measurements from the BAe-146 aircraft. The DLR Falcon showed a fine mode that was shifted to smaller sizes compared to that of the FAAM BAe-146 data, with a peak at a diameter of 0.12 μm. The coarse mode from the DLR Falcon data differed from that reported from the FAAM BAe-146 aircraft data, with the mass distribution peaking at a diameter of $\sim$10 μm, more than twice the peak diameter of the FAAM BAe-146 data. The coarse mode was also broader; the lognormal fit had a geometric standard deviation 2.5 compared to 1.8 for the FAAM BAe-146 lognormal fit. Even when particle shape and refractive index assumptions are aligned, the FAAM coarse-mode peak diameter was 4.5 μm which is still significantly smaller. It therefore appears the CAS and FSSP instruments may have differing sensitivities as a function of particle size.

[88] Although it has been reported elsewhere that the SO_2 gas may have been separate from the aerosol from Eyjafjallajökull [*Thomas and Prata*, 2011], in this specific case study SO_2 and ash mass were well correlated. As such SO_2 provided a useful tracer for the ash cloud and confirmation of its volcanic origin. From the FAAM BAe-146 data, an ash concentration of 1 mg m^{-3} corresponded to an average enhancement of 110 nmol mol^{-1} SO_2 on this occasion. The DLR Falcon observed an enhancement of 120 nmol mol^{-1} SO_2 per mg m^{-3} of ash.

[89] Strong correlations were also noted between the aerosol scattering coefficient measured by the nephelometer and the total aerosol mass measured by PCASP and CAS. The ratio between these quantities led to an implied specific scattering coefficient (k_{sca}) of 0.60–0.85 m^2 g^{-1} at 550 nm. Despite known deficiencies with the aerosol inlet serving the nephelometer, average k_{sca} of 0.70 m^2 g^{-1} derived in this way was in excellent agreement with the k_{sca} of 0.68 m^2 g^{-1} derived from the optical particle counter size distribution. The closure between these two techniques allows the nephelometer aerosol scattering coefficient to be used as an additional guide for deriving mass, provided an a-priori assumption of k_{sca} or knowledge of the size distribution. The Ångström exponent in the volcanic ash cloud covering 450 nm to 700 nm was estimated to be -0.3 from nephelometer data providing confirmation that large particles dominated the sample. This is lower than expected from

calculations based on particle size distribution measurements, which may suggest that some coarse-mode particles are in fact enhanced in the inlet and balance any losses of the largest coarse-mode particles. Further work is necessary to fully assess the particle size dependency of the characteristics of the Rosemount inlet.

[90] Reasonable internal closure has been demonstrated between the FAAM BAe-146 lidar and FAAM BAe-146 optical particles counter estimates of aerosol extinction and mass concentration using common assumptions for the refractive index, shape and density. Applying a mass specific extinction coefficient derived from the CAS and PCASP size distribution to the lidar extinction data provides mass concentration estimates and total column mass loadings that are in agreement with those calculated from the in situ CAS and PCASP profile measurements.

[91] This study highlights the value of combining measurements from optical particle counters, a three wavelength nephelometer and SO_2 analyzer, in particular when enhanced with a lidar to provide a larger-scale view. The high spatial variability of volcanic ash is clearly demonstrated; the lidar data suggests that the column loading varies by around a factor of three over length scales of around 100 km. This demonstrates some of the problems faced by numerical models such as NAME which are unable to capture such variability explicitly over small spatial scales. Although the NAME model predicted peak atmospheric concentrations of volcanic ash between 200 and 2000 μg m^{-3} across much of the southern North Sea, most of the work described in this paper occurred in a narrow strip where NAME indicated peak ash concentrations <200 μg m^{-3}. This suggests that there were small positional errors (approximately 50 km) in the westward extent of the ash cloud over the North Sea. The forecast ash over land areas of the UK was not detected in the lidar measurements highlighting the difficulties in forecasting such events and demonstrating the essential nature of high quality in situ and remote sensing validation data from observational platforms such as the FAAM BAe-146 and DLR Falcon.

[92] **Acknowledgments.** Airborne data were obtained using the BAe-146-301 Atmospheric Research Aircraft flown by Directflight Ltd. and managed by the Facility for Airborne Atmospheric Measurements (FAAM), which is a joint entity of the Natural Environment Research Council and the Met Office. Thanks are due to all at FAAM, Directflight, Avalon and BAe Systems whose dedication made this work possible. The CAPS instrument was provided through the Facility for Ground-based Atmospheric Measurement (FGAM) by Martin Gallagher, Hugh Coe and James Dorsey at the Centre for Atmospheric Science, University of Manchester. EUMETSAT are thanked for provision of SEVIRI imagery and the Met Office Atmospheric Dispersion team for NAME model output. We thank Roland Doerffer, Gerrit de Leeuw and Christian Hermans for their effort in establishing and maintaining Helgoland, Cabauw and Brussels AERONET sites as well as Brent Holben and his team for maintaining the infrastructure and data quality and processing.

References

Anderson, T. L., and J. A. Ogren (1998), Determining aerosol radiative properties using the TSI3563 integrating nephelometer, *Aerosol Sci. Technol.*, *29*(1), 57–69, doi:10.1080/02786829808965551.

Ansmann, A., et al. (2010), The 16 April 2010 major volcanic ash plume over central Europe: EARLINET lidar and AERONET photometer observations at Leipzig an Munich, Germany, *Geophys. Res. Lett.*, *37*, L13810, doi:10.1029/2010GL043809.

Balkanski, Y., M. Schulz, T. Claquin, and S. Guibert (2007), Reevaluation of mineral aerosol radiative forcings suggests a better agreement with satellite and AERONET data, *Atmos. Chem. Phys.*, *7*, 81–95, doi:10.5194/acp-7-81-2007.

Baumgardner, D., H. Jonsson, W. Dawson, D. O'Connor, and R. Newton (2001), The cloud, aerosol and precipitation spectrometer: A new instrument for cloud investigations, *Atmos. Res.*, *59–60*, 251–264, doi:10.1016/S0169-8095(01)00119-3.

Carn, S. A., et al. (2011), In situ measurements of tropospheric volcanic plumes in Ecuador and Colombia during TC4, *J. Geophys. Res.*, *116*, D00J24, doi:10.1029/2010JD014718.

Dubovik, O., et al. (2006), Application of spheroid models to account for aerosol particle nonsphericity in remote sensing of desert dust, *J. Geophys. Res.*, *111*, D11208, doi:10.1029/2005JD006619.

Francis, P. N., M. C. Cooke, and R. W. Saunders (2012), Retrieval of physical properties of volcanic ash using Meteosat: A case study from the 2010 Eyjafjallajökull eruption, *J. Geophys. Res.*, *117*, D00U09, doi:10.1029/2011JD016788.

Gerbig, C., S. Schmitgen, D. Kley, A. Volz-Thomas, K. Dewey, and D. Haaks (1999), An improved fast-response vacuum-UV resonance fluorescence CO instrument, *J. Geophys. Res.*, *104*(D1), 1699–1704, doi:10.1029/1998JD100031.

Guffanti, M., T. J. Casadevall and K. Budding (2010), Encounters of aircraft with volcanic ash clouds: A compilation of known incidents, 1953–2009, *U.S. Geol. Surv. Data Ser.*, *545*, 12 pp.

Haywood, J. M., P. Francis, O. Dubovik, M. Glew, and B. Holben (2003), Comparison of aerosol size distributions, radiative properties, and optical depths determined by aircraft observations and Sun photometers during SAFARI 2000, *J. Geophys. Res.*, *108*(D13), 8471, doi:10.1029/2002JD002250.

Haywood, J. M., B. T. Johnson, S. R. Osborne, J. Mulcahy, M. E. Brooks, M. A. J. Harrison, S. F. Milton, and H. E. Brindley (2011), Observations and modelling of the solar and terrestrial radiative effects of Saharan dust: A radiative closure case-study over oceans during the GERBILS campaign, *Q. J. R. Meteorol. Soc.*, *137*, 1211–1226, doi:10.1002/qj.770.

Hobbs, V. P., L. F. Radke, J. H. Lyons, R. J. Ferek, D. J. Coffman, and T. J. Casadevall (1991), Airborne measurements of particle and gas emissions from the 1990 volcanic eruptions of Mount Redoubt, *J. Geophys. Res.*, *96*(D10), 18,735–18,752, doi:10.1029/91JD01635.

Holben, B. N., et al. (1998), AERONET–A federated instrument network and data archive for aerosol characterization, *Remote Sens. Environ.*, *66*, 1–16, doi:10.1016/S0034-4257(98)00031-5.

Hopkins, J. R., R. K. Boddy, J. F. Hamilton, J. D. Lee, A. C. Lewis, R. M. Purvis, and N. J. Watson (2006), An observational case study of ozone and precursors inflow to southeast England during an anticyclone, *J. Environ. Monit.*, *8*(12), doi:10.1039/b608062f.

Horwell, C. J. (2007), Grain-size analysis of volcanic ash for the rapid assessment of respiratory health hazard, *J. Environ. Monit.*, *9*, 1107–1115, doi:10.1039/b710583p.

Hunton, D. E., et al. (2005), In-situ aircraft observations of the 2000 Mt. Hekla volcanic cloud: Composition and chemical evolution in the Arctic lower stratosphere, *J. Volcanol. Geotherm. Res.*, *145*, 23–34, doi:10.1016/j.jvolgeores.2005.01.005.

Johnson, B. T., and S. R. Osborne (2011), Physical and optical properties of mineral dust aerosol measured by aircraft during the GERBILS campaign, *Q. J. R. Meteorol. Soc.*, *137*, 1117–1130, doi:10.1002/qj.777.

Johnson, B. T., B. Heese, S. A. McFarlane, P. Chazette, A. Jones, and N. Bellouin (2008), Vertical distribution and radiative effects of mineral dust and biomass burning aerosol over west Africa during DABEX, *J. Geophys. Res.*, *113*, D00C12, doi:10.1029/2008JD009848.

Jones, A. R., D. J. Thomson, M. Hort, and B. Devenish (2007), The U.K. Met Office's next generation atmospheric dispersion model, NAME III, in *Air Pollution Modeling and its Application XVII (Proceedings of the 27th NATO/CCMS International Technical Meeting on Air Pollution Modelling and Its Application)*, edited by C. Borrego and A.-L. Norman, pp. 580–589, Springer, New York.

Kaye, G. W. C., and T. H. Laby (1995), Properties of inorganic compounds, in *Tables of Physical and Chemical Constants*, 16th ed., edited J. G. Noyes et al., pp. 223–238, Longman, Harlow, U. K.

Kristiansen, N. I., et al. (2012), Performance assessment of a volcanic ash transport model mini-ensemble used for inverse modelling of the 2010 Eyjafjallajökull eruption, *J. Geophys. Res.*, doi:10.1029/2011JD016844, in press.

Luke, W. T. (1997), Evaluation of a commercial pulsed fluorescent detector for the measurements of low-level SO_2 concentrations during the Gas-Phase Sulfur Intercomparison Experiment, *J. Geophys. Res.*, *102*(D13), 16,255–16,265, doi:10.1029/96JD03347.

Marenco, F., B. Johnson, K. Turnbull, S. Newman, J. Haywood, H. Webster, and H. Ricketts (2011), Airborne lidar observations of the 2010 Eyjafjallajokull volcanic ash plume, *J. Geophys. Res.*, *116*, D00U05, doi:10.1029/2011JD016396.

Millington, S. C., R. Saunders, P. Francis, and H. N. Webster (2012), Simulated volcanic ash imagery: A method to compare NAME ash concentration forecasts with SEVIRI imagery for the Eyjafjallajökull eruption in 2010, *J. Geophys. Res.*, doi:10.1029/2011JD016770, in press.

Newman, S., L. Clarisse, D. Hurtmans, F. Marenco, B. Johnson, K. F. Turnbull, S. Havemann, A. J. Baran, D. O'Sullivan, and J. M. Haywood (2012), A case study of observations of volcanic ash from the Eyjafjallajökull eruption: 2. Airborne and satellite radiative measurements, *J. Geophys. Res.*, doi:10.1029/2011JD016780, in press.

Oppenheimer, C., et al. (2010), Atmospheric chemistry of an Antarctic volcanic plume, *J. Geophys. Res.*, *115*, D04303, doi:10.1029/2009JD011910.

Osborne, S. R., and J. M. Haywood (2005), Aircraft observations of the physical and optical properties of major aerosol types, *Atmos. Res.*, *73*, 173–201, doi:10.1016/j.atmosres.2004.09.002.

Osborne, S. R., B. T. Johnson, J. M. Haywood, A. J. Baran, M. A. J. Harrison, and C. L. McConnell (2008), Physical and optical properties of mineral dust aerosol during the dust and biomass-burning experiment, *J. Geophys. Res.*, *113*, D00C03, doi:10.1029/2007JD009551.

Osborne, S. R., A. J. Baran, B. T. Johnson, J. M. Haywood, E. Hesse, and S. Newman (2011), Short-wave and long-wave radiative properties of Saharan dust aerosol, *Q. J. R. Meteorol. Soc.*, *137*(658), 1149–1167, doi:10.1002/qj.771.

Otto, S., E. Bierwirth, B. Weinzierl, K. Kandler, M. Esselborn, M. Tesche, A. Schladitz, M. Wendisch, and T. Trautmann (2009), Solar radiative effects of a Saharan dust plume observed during SAMUM assuming spheroidal model particles, *Tellus, Ser. B*, *61*(1), 270–296, doi:10.1111/j.1600-0889.2008.00389.x.

Patterson, E. M. (1981), Measurements of the imaginary part of the refractive index between 300 and 700 nanometers for Mount St. Helens ash, *Science*, *211*, 836–838, doi:10.1126/science.211.4484.836.

Patterson, E. M., C. O. Pollard, and I. Galindo (1983), Optical properties of the ash from El Chichon Volcano, *Geophys. Res. Lett.*, *10*(4), 317–320, doi:10.1029/GL010i004p00317.

Roberts, T. J., C. F. Braban, R. S. Martin, C. Oppenheimer, J. W. Adams, R. A. Cox, R. L. Jones, and P. T. Griffiths (2009), Modelling reactive halogen formation and ozone depletion in volcanic plumes, *Chem. Geol.*, *263*(1–4), 151–163, doi:10.1016/j.chemgeo.2008.11.012.

Rose, W. I., et al. (2006), Atmospheric chemistry of a 33–34 hour old volcanic cloud from Hekla Volcano (Iceland): Insights from direct sampling and the application of chemical box modeling, *J. Geophys. Res.*, *111*, D20206, doi:10.1029/2005JD006872.

Schumann, U., et al. (2011), Airborne observations of the Eyjafjalla Volcano ash cloud over Europe during air space closure in April and May 2010, *Atmos. Chem. Phys.*, *11*, 2245–2279, doi:10.5194/acp-11-2245-2011.

Thomas, H. E., and A. J. Prata (2011), Sulphur dioxide as a volcanic ash proxy during the April–May 2010 eruption of Eyjafjallajökull Volcano, Iceland, *Atmos. Chem. Phys.*, *11*, 6871–6880, doi:10.5194/acp-11-6871-2011.

Vance, A., A. J. S. McGonigle, A. Aiuppa, J. L. Stith, K. Turnbull, and R. von Glasow (2010), Ozone depletion in tropospheric volcanic plumes, *Geophys. Res. Lett.*, *37*, L22802, doi:10.1029/2010GL044997.

von Glasow, R. (2010), Atmospheric chemistry in volcanic plumes, *Proc. Natl. Acad. Sci. U. S. A.*, *107*, 6594–6599, doi:10.1073/pnas.0913164107.

Webley, P., and L. Mastin (2009), Improved prediction and tracking of volcanic ash clouds, *J. Volcanol. Geotherm. Res.*, *186*, 1–9, doi:10.1016/j.jvolgeores.2008.10.022.

Webster, H. N., et al. (2012), Operational predication of ash concentrations in the distal volcanic cloud from the 2010 Eyjafjallajökull eruption, *J. Geophys. Res.*, *117*, D00U08, doi:10.1029/2011JD016790.

Weinzierl, B., A. Petzold, M. Esselborn, M. Wirth, K. Rasp, K. Kandler, L. Schütz, P. Koepke, and M. Fiebig (2009), Airborne measurements of dust layer properties, particle size distribution and mixing state of Saharan dust during SAMUM 2006, *Tellus, Ser. B*, *61*, 96–117, doi:10.1111/j.1600-0889.2008.00392.x.

Weinzierl, B., et al. (2011), Microphysical and optical properties of dust and tropical biomass burning aerosol layers in the Cape Verde region: An overview of the airborne in situ and lidar measurements during SAMUM-2, *Tellus, Ser. B*, *63*, 589–618, doi:10.1111/j.1600-0889.2011.00566.x.

Witham, C. S., H. N. Webster, M. C. Hort, A. R. Jones, and D. J. Thomson (2012), Modelling concentrations of volcanic ash encountered by aircraft in past eruptions, *Atmos. Environ.*, doi:10.1016/j.atmosenv.2011.06.073, in press.

J. Haywood, College of Engineering, Mathematics, and Physical Science, University of Exeter, Exeter EX4 4QF, UK.

B. Johnson, F. Marenco, and K. Turnbull, Observation Based Research, Met Office, Fitzroy Road, Exeter EX1 3PB, UK. (kate.turnbull@metoffice.gov.uk)

S. Leadbetter, Atmospheric Dispersion, Met Office, Fitzroy Road, Exeter EX1 3PB, UK.

A. Minikin, H. Schlager, U. Schumann, and B. Weinzierl, Institut für Physik der Atmosphäre, DLR, Oberpfaffenhofen, Wessling D-82234, Germany.

A. Woolley, FAAM, Cranfield MK43 0AL, UK.